INFLUENCE OF WETTABILITY ON BOILING HEAT TRANSFER AND CRITICAL HEAT FLUX IN VERTICAL FLOW BOILING

BY

JOSEPH L. BOTTINI

THESIS

Submitted in partial fulfillment of the requirements
for the degree of Master of Science in Nuclear, Plasma, and Radiological Engineering
in the Graduate College of the
University of Illinois at Urbana-Champaign, 2018

Urbana, Illinois

Master's Committee:

Assistant Professor Caleb S. Brooks
Associate Professor Tomasz Kozlowski

ABSTRACT

The critical heat flux (CHF) marks the upper limit of safe operation of heat transfer systems that utilize two-phase boiling heat transfer. In a heat-flux-controlled system, exceeding the CHF results in rapid temperature excursions which can be catastrophic for system components. In nuclear power generation, the initiation of a CHF event may cause fuel damage through fuel melting or through zircaloy oxidation. CHF marks the upper limit for safe reactor operation in light-water reactor systems. The understanding of the physical triggering mechanisms for CHF and the accurate prediction of CHF values is important not only for safe reactor operation, but also for efficient plant design and effective fuel utilization. Gamma radiation present in commercial nuclear reactors may affect the surface wettability of fuel rods through the Radiation Induced Surface Activation (RISA) effect, and present power limits on nuclear reactors may be underestimated. Recent studies have focused on the influence of surface wettability on the departure from nucleate boiling (DNB) through surface modifications and coatings, though many of these studies are limited to pool boiling systems.

In this thesis, the surface wettability influence is studied on the boiling curves and specifically the point of DNB. A femtosecond laser is used to texture the surface to change the wettability from hydrophilic to hydrophobic. A parametric study is performed with mass flux, pressure, and inlet subcooling in a vertical rectangular channel that is heated from one side. CHF excursions are triggered under various system conditions and are compared with existing models. For the experimental conditions considered, the hydrophobic surface showed delayed onset of nucleate boiling compared to the hydrophilic surface, shifting the boiling curves to higher wall superheat. The hydrophobic surface also showed significantly lower CHF for the same system

conditions and less sensitivity to changes in subcooling. Few models accurately predicted the initiation of CHF, and a more conservative model is needed that more accurately incorporates the effect of surface wettability.

ACKNOWLEDGEMENTS

This material is based upon work supported under an Integrated University Program Graduate Fellowship, DOE Phase II SBIR/STTR (award number DE-SC0011851), and Starfire Industries LLC.

I would especially like to thank Caleb Brooks, my advisor, for his support, guidance, and patience on this project. I am grateful to Vineet Kumar for his assistance in performing the experiments necessary for this work. I would like to thank Sabrina Hammouti for her work in preparing the textured surface. I would also like to thank David Ruzic and Brian Jurczyk for their collaboration, providing the tools and facilities necessary for the surface preparation.

Finally, I would like to thank the members of my committee, Tomasz Kozlowski and Rizwan Uddin, for taking the time to review and critique my manuscript.

TABLE OF CONTENTS

NOMENCLATURE

A	area	(m^2)
c	specific heat	(J/kg-°C)
D	diameter	(m)
G	mass flux	(kg/m^2-s)
g	gravitational acceleration	(m/s^2)
h	enthalpy	(J/kg)
k	thermal conductivity	(W/m-°C)
L	length	(m)
P	pressure	(kPa)
Pr	Prandtl number	(Pr)
q	heat flux	(kW/m^2)
Re	Reynolds number	(-)
r	roughness factor	(-)
T	temperature	(°C)
ΔT	superheat or subcooling	(°C)
t	time	(s)
V	velocity	(m/s)
x	quality	(-)

Greek

ϵ	error	(-)
θ	contact angle	(°)

λ	Laplace length	(m)
ρ	density	(kg/m^3)
$\Delta\rho$	density difference	(kg/m^3)
σ	surface tension	(N/m)
σ_ψ	uncertainty in ψ	(units of ψ)
ϕ	orientation	(°)

Superscripts

*	non-dimensionalized quantity

Subscripts

b	intercept
CHF	critical heat flux
exp	experimental
FC	forced convection
f	liquid phase
fg	vaporization phase change
g	vapor phase
H	heated
h	hydraulic
i	inlet
MX	MX 9000 signal processor
m	spatial temperature slope
mod	model
NI	National Instruments

PB	pool boiling
PT	pressure transducer
p	constant pressure
phil	hydrophilic
phob	hydrophobic
sub	subcooling
TC	thermocouple
TF	turbine flowmeter
w	wall

CHAPTER 1: INTRODUCTION

Boiling heat transfer is an effective cooling mechanism whereby large amounts of heat are removed from critical system components through the heating and vaporization of coolant, either driven by a pump or through buoyant forces. Boiling heat transfer offers high heat transfer coefficients due to both the sensible heating and the latent heating of the coolant, enabling high steady-state cooling rates with minimal surface superheats. However, a concern of two-phase heat transfer not present in single-phase heat transfer is the transition to poor heat transfer region, particularly the departure from nucleate boiling (DNB) to film boiling in low-quality flows and the dryout of the annular film in high-quality flows, as shown in Figure 1.1. These transitions are characterized by sudden temperature excursions which risk damage to components. For this reason, the critical heat flux (CHF) is a major safety concern in boiling heat transfer as well as a limitation for effective heat removal in many engineering applications. Due to the complexity of the phenomenon, the accurate prediction of CHF remains a concern (Mishima and Nishihara, 1987; Chun et al., 2001; Shoesse et al., 1997; El-Genk et al., 1988; Park et al., 1998; Kim et al., 2000; Lu et al., 2014; Mayer et al., 2016; Lin and Chen, 2012).

Two-phase heat transfer is typically characterized by a boiling curve in terms of the wall heat flux, q''_w, and the wall superheat, ΔT_w, defined as the difference between the wall temperature, T_w, and the fluid saturation temperature, T_{sat}. A sample, qualitative pool boiling curve is shown in Figure 1.2. Although the curve shown is for pool boiling, the differences between pool boiling and flow boiling are minor for DNB-type CHF excursions. The first region is the single-phase convection region where the wall superheat is not sufficient to initiate boiling at the heater surface. In the pool boiling case, the single-phase region is driven by natural convection; in

flow boiling, the flow is the driving force. Point (a) marks the separation between the single-phase convection and the two-phase boiling region, referred to as the onset of nucleate boiling (ONB) point. Beyond this point, the heat transfer is increased due to the supplementation of latent heating to the sensible heating. In contrast, only sensible heating is present in single-phase heat transfer.

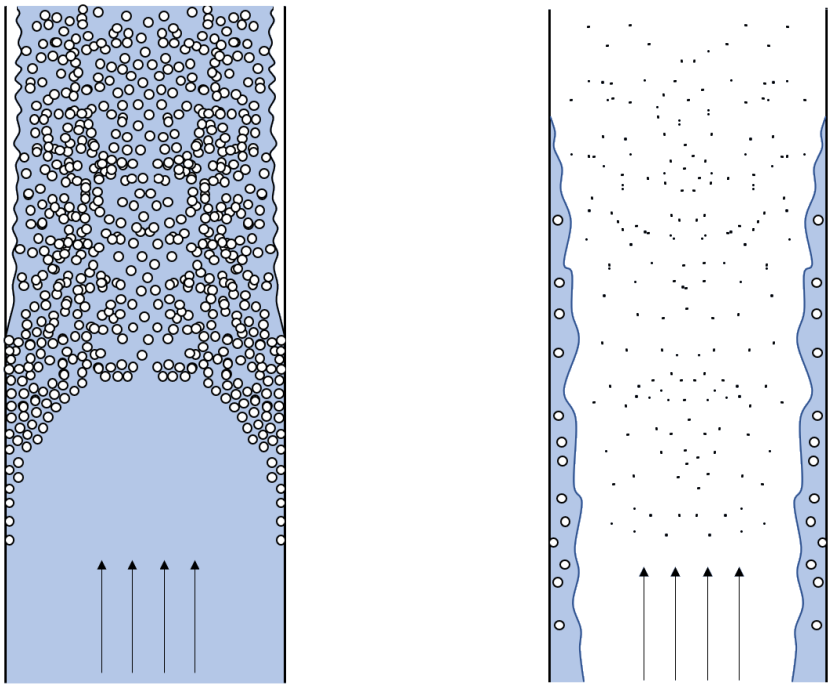

Figure 1.1 Two types of boiling crisis present in two-phase heat transfer: (a) departure from nucleate boiling, and (b) annular film dryout (based on Duderstadt and Hamilton, 1976)

In the nucleate boiling region, bubbles are formed and depart from the heater surface and mix with the flow. As the wall temperature and heat flux increase, the rate at which bubbles form on the heater surface increases, and, therefore, the heat transfer efficiency increases. However, at point (c), the heat transfer efficiency peaks, and beyond this point, the heat transfer coefficient begins to decrease. The decrease in heat transfer efficiency is due to the overcrowding of vapor on the heater surface which acts as an insulating layer due to the lower thermal conductivity of vapor compared to liquid. The point at which this occurs is the Departure from Nucleate Boiling (DNB)

point and is characterized by the Critical Heat Flux (CHF), q''_{CHF}. Beyond this point, the two-phase heat transfer is characterized as partial film boiling or transition boiling.

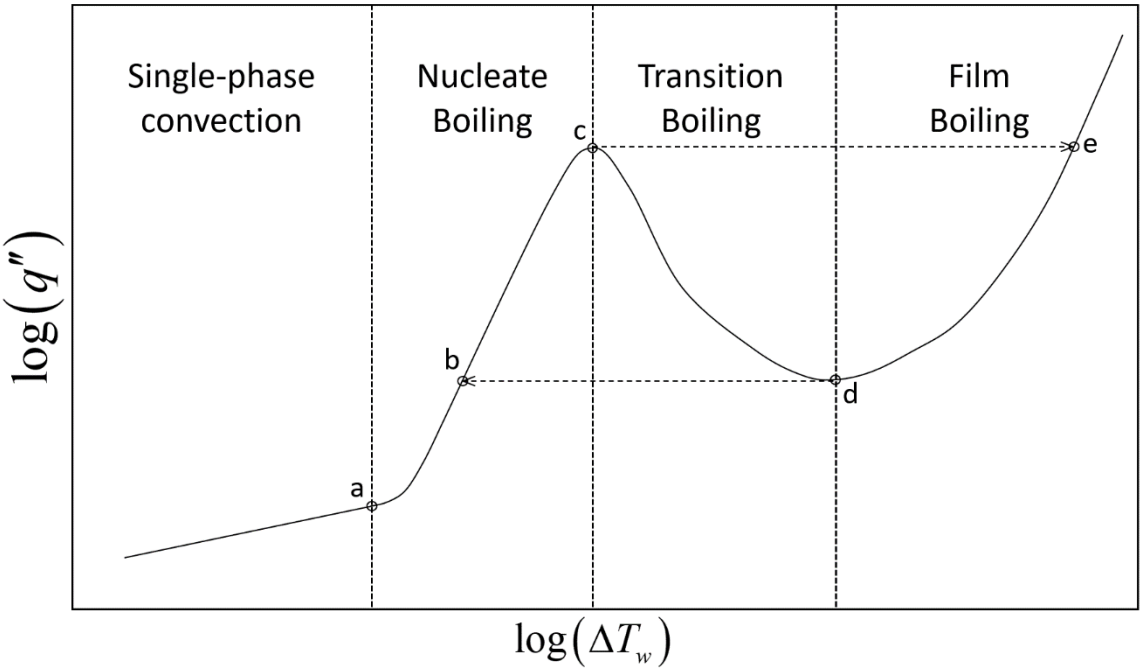

Figure 1.2 Sample, qualitative pool boiling curve showing the four regions of two-phase heat transfer (based on Duderstadt and Hamilton, 1976)

Transition boiling is the intermediate between nucleate and film boiling where vapor envelops the heater surface, but liquid is still able to periodically wet the surface. The region is marked by two points: the CHF point at the right-hand extreme of the nucleate boiling region (point c), and the Leidenfrost point at the left-hand extreme of the film boiling region (point d). The Leidenfrost point is characterized by the Leidenfrost temperature which is the minimum surface superheat needed to maintain a continuous vapor layer at the heater surface. Beyond the Leidenfrost temperature is the fourth region, film boiling, which has poor heat transfer due to the insulating effect of the vapor layer. Wall superheat can become very large in this region due to the increase in radiative heat transfer from high wall temperatures.

In temperature-controlled systems, the effect of DNB is only seen as a deterioration of the heat transfer beyond a certain wall superheat. The boiling crisis and the deterioration of heat transfer in temperature-controlled systems do not cause damage to system components. However, in power-controlled systems, the effects can be catastrophic. If the critical heat flux is exceeded, a rapid change to poor-quality heat transfer is initiated, characterized by a substantial increase in the wall temperature – shown as point (c) to point (e) in Figure 1.2. In order to reverse the transition, the heat flux must drop below the heat flux at the Leidenfrost point, a value which is much lower than the CHF point. Only at this point does the vapor layer collapse and return to nucleate boiling where the heat transfer is efficient – shown as a transition from point (d) to point (b) in Figure 1.2.

The transition to poor-quality heat transfer is of major interest in the nuclear power industry. In pressurized water reactors, although the flow is subcooled, vapor is still generated within the reactor core, and DNB is a concern. In boiling water reactors, although DNB is less of a hazard, the dryout of the annular film is a major concern, both marking the CHF of the reactor system. Current nuclear power systems use fuel rods with a uranium dioxide fuel, a zircaloy cladding, and a helium gap between the two. While the thermal conductivity of the zircaloy is high, the thermal conductivities of the helium gas and the ceramic fuel are low. Combined with a large heat generation rate in the fuel elements, the centerline temperatures of the fuel elements can reach in excess of 2000°C. Two major safety criteria for the design of nuclear reactors is the integrity of the fuel elements and the prevention of zircaloy oxidation which generates hydrogen within the reactor core. The integrity of the fuel elements is partially characterized by the melting temperature of UO_2, 2800°C, and the oxidation of zircaloy cladding in water, which occurs around 800-1200°C. If a CHF event is encountered, either of these two phenomena may occur which poses great risk for safe reactor operation. The initiation of CHF is, therefore, the current power-limiting

design criterion for many nuclear reactors, and the accurate prediction of CHF is important not only for reactor safety, but for efficient plant design as well. CHF has, therefore, been widely studied and applied to the nuclear power industry.

1.1 Existing Work

Many models exist in order to fundamentally explain the triggering mechanism for CHF. These include the Hydrodynamic Instability Model (Zuber, 1959; Sakashita and Ono, 2009; Lienhard and Dhir, 1973) the Near-Wall Bubble Crowding Model (Hebel et al., 1981; Weisman and Pei, 1983), the Liquid Sublayer Dryout Model (Haramura and Katto, 1983; Lee and Mudawar, 1988; Celata et al., 1994), and others (Kolev, 2009; Wang and Dhir, 1993). Many studies have been conducted to experimentally measure and improve prediction of the critical heat flux in conditions relevant to commercial power generation (Weatherhead, 1963; Bergles, 1964; Weisman, 1983; Hall and Mudawar, 2000). Particular attention has been given to addressing difficulties under low-pressure, low-flow conditions. Mishima and Nishihara (1987) analyzed the effect different geometries had on the CHF phenomenon, studying annuli, pipes, and square channels. For low-flow conditions, the CHF was found to approach the flooding limit due to countercurrent-flow limitation proposed by Wallis (1961) where the flow geometry was captured by a single constant. Chun et al. (2001) and Schoesse et al. (1997) also observed that the lower limit of CHF was captured by the flooding condition, and that subcooling and pressure were less influential on the CHF in this low-flow regime. El-Genk et al. (1988), Park et al. (1998), and Kim et al. (2000) all observed that beyond the flooding limit (i.e., flow rates greater than 100-150 kg/m^2-s) the CHF increased with increasing pressure, mass flux, and subcooling. This effect was also observed by Chun et al. (2001) which considered a wide range of pressures for CHF under low

flow, observing that the peak in CHF occurred between 2 and 3 MPa. Park et al. (1998) and Kim et al. (2000) both observed that the CHF also increased with increasing channel diameter and with decreasing heated length at constant mass flux. Lu et al. (2014) and Mayer et al. (2016) observed that the critical equilibrium quality decreased with increasing mass flux and decreasing pressure. Many studies that compared CHF data with existing models conclude that more research on CHF under low-pressure, low-flow conditions is required. Several models of CHF are given below in Table 1.1.

In addition to system parameters such as flow rate, pressure, diameter, and inlet subcooling, much effort has been devoted in recent years to surface effects on boiling heat transfer and critical heat flux. Frost and Kippenhan (1967) first showed the influence of surface tension on boiling heat transfer by adding surface active agents to the bulk fluid in order to reduce surface tension at the heater surface, yielding an enhancement of the heat transfer. Kandlikar (2001) developed a pool boiling model that incorporated the influence of surface wettability using data on vertical pool boiling with multiple wettability surfaces and working fluids. The developed model is an adaptation of Zuber's (1959) model with coefficients involving contact angle. However, the predicted value for CHF decreases to zero as the contact angle approaches 180°. Hsu and Chen (2012) studied the effect wettability had on boiling heat transfer with nano-silica particle coatings on a copper surface in a horizontal pool boiling system. The CHF was observed to decrease with increasing contact angle, and pool boiling curves shifted to greater wall superheat with increasing contact angle, thus degrading the heat transfer in the nucleate boiling regime. Large differences were also observed in the wall nucleation phenomenon between the different wettability surfaces. Li et al. (2013) performed a theoretical analysis and an experimental study on the influence of

Table 1.1 Summary of important CHF models

Work	Model
Zuber (1952)	$q''_{CHF} = Kh_{fg}\rho_g^{1/2}\left[\sigma\Delta\rho g\right]^{1/4}, \quad K = 0.11-0.13$
Mirshak et al. (1959)	$q''_{CHF} = 1.51\times10^{6}\left(1+0.1197U_m\right)\left(1+9.14\times10^{-3}\Delta T_{sub}\right)\left(1+1.896P\right)$
Wallis (1961)	$q''_{CHF} = \dfrac{A}{A_H}\dfrac{C^2 h_{fg}\sqrt{\rho_g g\Delta\rho D}}{\left[1+\left(\rho_g/\rho_l\right)^{1/4}\right]^2}$
Biasi (1967)	$q''_{CHF} = \begin{cases} q''_1, & \text{G} < 300\ \text{kg/m}^2\text{-s} \\ \max\left(q''_1, q''_2\right), & \text{G} > 300\ \text{kg/m}^2\text{-s} \end{cases}$ $q''_1 = 2.764\times10^{7}\left(100D\right)^{-n} G^{-1/6}\left[1.468F\left(p_b\right)G^{-1/6} - x\right]\text{W/m}^2$ $q''_2 = 15.048\times10^{7}\left(100D\right)^{-n} G^{-0.6}H\left(p_b\right)\left[1-x\right]\text{W/m}^2$ $F\left(p_b\right) = 0.7249 + 0.099\,p_b\exp\left(-0.032\,p_b\right)$ $H\left(p_b\right) = -1.159 + 0.149\,p_b\exp\left(-0.019\,p_b\right) + 9\,p_b\left(10+p_b^2\right)^{-1}$
Bowring (1972)	$q''_{CHF} = \dfrac{A - Bh_{fg}x}{C}\text{W/m}^2, \quad A = \dfrac{2.317\left(h_{fg}DG/4\right)F_1}{1+0.0143F_2D^{1/2}G},$ $B = \dfrac{DG}{4}, \qquad C = \dfrac{0.077\,f_3DG}{1+0.347F_4\left(\dfrac{G}{1356}\right)^n},$ $n = 2.0 - 0.5\,p_R, \qquad p_R = 0.145\,p,$ $\left.\begin{aligned} F_1 &= p_R^{-0.368}\exp\left[0.648\left(1-p_R\right)\right] \\ F_2 &= F_1 / \left\{p_R^{-0.448}\exp\left[0.245\left(1-p_R\right)\right]\right\} \\ F_3 &= p_R^{0.219} \\ F_4 &= F_3 p_R^{1.649} \end{aligned}\right\} \quad p_R > 1\text{MPa}$
Thorgerson et al. (1974)	$q''_{CHF} = \left(q''_{PB} + q''_{FC}\right)$ $q''_{PB} = 0.15h_{fg}\rho_g\left[\dfrac{\sigma\Delta\rho}{\rho_g^2}\right]^{-0.25}\left[1+\dfrac{\left(\rho_l/\rho_g\right)^{0.923}c_p\Delta T_{sub}}{25h_{fg}}\right]$ $q''_{FC} = 0.023\dfrac{k_l}{D_e}\text{Re}^{0.8}\,\text{Pr}^{0.4}\left(57\ln P - \dfrac{54P}{P+0.1034} - \dfrac{V}{122} - T_c\right)$

Table 1.1 Continued

Katto (1981)	$q''^{*}_{CHF} = \min\left(0.25 D_h G^* / L, C_1\left(\frac{D_h}{L}\right)\left[\frac{1}{L}\sqrt{\frac{\sigma}{\rho_l}}\left(\frac{\rho_l}{\rho_g}\right)\frac{1}{G^{*2}}\right]^{0.043} G^*\right)$, low flow $q''^{*}_{CHF} = \frac{0.1\left(\rho_l/\rho_g\right)^{0.2}\left(G^*\sqrt{\sigma/\rho_l}\right)^{1/2}}{1+0.0031\left(L/D_h\right)}$, high flow $q''^{*}_{CHF} = \frac{q''_{CHF}}{h_{fg}\sqrt{\lambda\rho_g\Delta\rho g}}, \quad G^* = \frac{G}{\sqrt{\lambda\rho_g\Delta\rho g}}, \quad \lambda = \sqrt{\frac{\sigma}{\Delta\rho g}}$ $C_1 = 0.25 \quad L/D_h < 50$ $C_1 = 0.25 + 0.0009\left(L/D_h - 50\right) \quad 50 \le L/D_h < 150$ $C_1 = 0.34 \quad L/D_h \ge 150$
Mishima et al. (1983)	$q''^{*}_{CHF} = \left(\frac{A}{A_H}\right)\left(\frac{\Delta h_i}{h_{fg}}\right)G^* + 0.7\left(\frac{A}{A_H}\right)\frac{\sqrt{D/\lambda}}{\left[1+m\left(\rho_G/\rho_l\right)^{1/4}\right]^2}$ $q''^{*}_{CHF} = \frac{q''_{CHF}}{h_{fg}\sqrt{\lambda\rho_g\Delta\rho g}}, \quad \lambda = \sqrt{\frac{\sigma}{\Delta\rho g}}$
Mishima and Ishii (1984)	$q''^{*}_{CHF} = q''^{*}_{cF} + \frac{A}{A_H}\frac{\Delta h_i}{h_{fg}}G^* \qquad q''_{cF} = \frac{A}{A_H}\frac{C^2 h_{fg}\sqrt{\rho_g g\Delta\rho D}}{\left[1+\left(\rho_g/\rho_l\right)^{1/4}\right]^2}$ $q''^{*}_{CHF} = \frac{q''_{CHF}}{h_{fg}\sqrt{\lambda\rho_g\Delta\rho g}} \qquad G^* = \frac{G}{\sqrt{\lambda\rho_g\Delta\rho g}} \qquad \lambda = \sqrt{\frac{\sigma}{\Delta\rho g}}$
Sudo et al. (1985)	$q''^{*}_{CHF} = \max\left(q''^{*}_1, q''^{*}_2, q''^{*}_3\right),$ $q''^{*}_1 = 0.7\frac{A}{A_H}\frac{\sqrt{D/\lambda}}{\left[1+\left(\rho_g/\rho_f\right)^{1/4}\right]^2}, \quad q''^{*}_2 = 0.005\left\lvert G^*\right\rvert^{0.611}, \quad q''^{*}_3 = \frac{A}{A_H}\frac{\Delta h_i}{h_{fg}}G^*,$ $q''^{*}_{CHF} = \frac{q''_{CHF}}{h_{fg}\sqrt{\lambda\rho_g\Delta\rho g}}, \qquad G^* = \frac{G}{\sqrt{\lambda\rho_g\Delta\rho g}}, \qquad \lambda = \sqrt{\frac{\sigma}{\Delta\rho g}}$
Kandlikar (2001)	$q''_{CHF} = K h_{fG}\rho_g^{1/2}\left[\sigma\Delta\rho g\right]^{1/4}$ $K = \left(\frac{1+\cos\theta}{16}\right)\left[\frac{2}{\pi}\left(1-\sqrt{\phi_s}\right)^{-1/2}\frac{r+\cos\theta}{1+\cos\theta} + \frac{\pi}{4}\left(1-\sqrt{\phi_s}\right)^{1/2}\left(1+\cos\theta\right)\cos\phi\right]^{1/2}$

Table 1.1 Continued

Ahn et al. (2011)	$q''_{CHF} = q''_{Kand} + q''_w$ $q''_{Kand} = Sh_{fg}\rho_g^{1/2}\left[\sigma\Delta\rho g\right]^{1/4}\left(\frac{1+\cos\theta}{16}\right)\left[\frac{2}{\pi}+\frac{\pi}{4}(1+\cos\theta)\cos\phi\right]^{1/2}$ $q''_w = \frac{\epsilon\delta\rho_l h_{fg} K}{A_{heat}}\frac{dA_w}{dt}$
Chu et al. (2012)	$q''_{CHF} = h_{fg}\rho_g^{1/2}\left[\sigma\Delta\rho g\right]^{1/4}\left(\frac{1+\cos\theta}{16}\right)\times\left[\frac{2}{\pi}\frac{1+r\cos\theta_{rec}}{1+\cos\theta}+\frac{\pi}{4}(1+\cos\theta)\cos\phi\right]^{1/2}$
Quan et al. (2014)	$q''_{CHF} = Kh_{fG}\rho_g^{1/2}\left[\sigma\Delta\rho g\right]^{1/4}$ $K = \left(\frac{1+\cos\theta}{16}\right)\left[\frac{2}{\pi}\left(1-\sqrt{\phi_s}\right)^{-1/2}\frac{r+\cos\theta}{1+\cos\theta}+\frac{\pi}{4}\left(1-\sqrt{\phi_s}\right)^{1/2}(1+\cos\theta)\cos\phi\right]^{1/2}$
Lu et al. (2014)	$q''^{*}_{CHF} = 0.0054G^{*0.69}e^{-0.0012L/D}$ $q''^{*}_{CHF} = \frac{q''_{CHF}}{h_{fg}\sqrt{\lambda\rho_g\Delta\rho g}}$ $G^{*} = \frac{G}{\sqrt{\lambda\rho_g\Delta\rho g}}$ $\lambda = \sqrt{\frac{\sigma}{\Delta\rho g}}$

wettability on boiling properties in pool conditions for hydrophilic surfaces. A semi-analytical model employing correlations involving wettability for the departure frequency, diameter, and site density were used to calculate the latent heating of the heater surface, and the model was shown to predict the heat flux within 30% for several hydrophilic surface wettabilities in pool boiling. Bourdon et al. (2013) also studied the influence of wettability on boiling heat transfer and onset of nucleate boiling, performing horizontal pool boiling studies on smooth glass surfaces. The wettability was controlled with chemical grafting, thereby not modifying the surface topography, obtaining two surfaces: hydrophilic and hydrophobic. The less wetted (hydrophobic) surface was found to have an earlier ONB point compared with the other surface, and the pool boiling curve was found to be shifted to lower wall superheat, though CHF was not investigated. Betz et al. (2013) studied the heat transfer and wall nucleation on superhydrophobic, superhydrophilic, biphilic, and superbiphilic surfaces under pool boiling. The surfaces were prepared using silicon wafers and oxygen plasma to make the surfaces superhydrophilic. A thin layer of Teflon

fluoropolymer was then spun onto select surfaces to create a superhydrophobic finish. It was observed that the nucleation site density increased with decreasing wettability (increasing contact angle) for the same wall superheat, which indicated an enhancement of the heat transfer coefficient for hydrophobic and superhydrophobic surfaces, a finding confirmed by the reported pool boiling curves. Jo et al. (2011) also observed a similar effect on the pool boiling curves with a higher heat transfer coefficient for hydrophobic surfaces at low wall superheat and a higher heat transfer coefficient for hydrophilic surfaces at high wall superheat. The surfaces were prepared in a similar manner to those by Betz et al. (2013) using a silicon dioxide surface for the hydrophilic surface and a Teflon surface for the hydrophobic surface. Both Betz et al. (2013) and Jo et al. (2011) observed lower CHF values for hydrophobic surfaces compared with hydrophilic surfaces and an enhancement of the CHF for biphilic or mixed-wettability surfaces. Marcel et al. (2017) modeled the effect wettability has on the boiling characteristics through contact angle and the departure diameter using a stochastic-automata model in pool boiling. The nucleation site density is greater at the same wall superheat for less wetting surfaces which causes the heat flux to be greater. Kim et al. (2017) studied the effect of surfaces with temperature varying wettabilities on the boiling heat transfer in vertical flow. Surfaces that became more hydrophilic at higher temperatures had boiling curves shifted to lower wall superheat. Kumar et al. (2014) observed the opposite trend, decreasing wettability shifts boiling curves to lower wall superheat using copper surfaces coated with diamond or carbon nanotubes thus changing the wettability. The CHF increased with increasing flow rate, but also increased with the carbon nanotube surface which has a lower wettability than the plain copper surface, an effect not observed by previous studies. A summary of experimental works employing surface modifications and wettability investigations is shown in Table 1.2.

Table 1.2 Experimental CHF studies with surface and wettability modifications

Work	Geometry	Material	Fluid	Contact Angle	Surface Modification	Pressure (kPa)	Subcooling (°C)	Flow Rate (kg/m^2-s)
Frost and Kippenhan (1967)	Vertical annulus, D_i=4.76 mm, D_o=38.1 mm, L_h=381 mm	Brass	Water	N/A	Surface Active Agent to reduce surface tension	207	44, 64, 83	0.24, 0.61, 1.22 m/s
Hsu and Chen (2012)	1.6 cm × 1.6 cm	Copper	Water	<10°, 16°, 25°, 75°, 132°, 145°	Nano-silica particles, fluoro-containing materials	101	0	N/A, pool
Li et al. (2013)	Cylinder, D=40mm, L=120 mm	Copper	Water	0°, 30°, 50°	TiO_2 coating	101	0	N/A, pool
Bourdon et al. (2013)	N/A	Glass	Water	0°, 114°	UV, O_3, OTS (Octadecyl-trichloro-silane)	101	0	N/A, pool
Betz et al. (2012)	1 cm × 3 cm	Silicon, indium tin dioxide	Water	7°, 20°, 120°, biphilic,	DRIE and oxygen plasma, Teflon®	101	0	N/A, pool
Jo et al. (2011)	25 mm × 20 mm	SiO_2	Water	54°, 123°	Teflon®	101	0	N/A, pool
Kim et al. (2017)	D_h=7.5mm, 10×15 mm^2	TiO_2, ZnO	Water	57°, 83°, 90°	SiO_2, TiO_2, ZnO	101	2-4	600-1200 kg/m^2-s
Kumar et al. (2014)	25×20 mm^2	Copper	Water	55°, 90°, 134°	Carbon Nanotube, Diamond, Sand-blasted copper	101	0	95-430 kg/m^2-s

1.2 Objectives

From a review of literature, although some effort has been made in pool conditions, few studies have systematically analyzed the effect of wettability on heat transfer and CHF in flow boiling. The objectives of this thesis are to meet the data needs for improved understanding of the influence of surface wettability on heat transfer and CHF in flow boiling, and evaluate the prediction capability of existing CHF models. This is accomplished by characterizing the effect of various system parameters on the boiling properties and CHF values for a hydrophilic surface and comparing them to the effects on a hydrophobic surface. The hydrophilic surface is a polished copper surface studied over a range of pressure, mass flux, and inlet subcooling values up to CHF. The hydrophobic surface is a laser-textured copper surface utilizing Laser Induced Periodic Surface Structures (LIPSS) to make the surface less wetting.

CHAPTER 2: EXPERIMENTAL APPROACH

The influence of surface wettability is evaluated experimentally by performing various flow boiling experiments. The influence of flow parameters such as pressure, flow rate, and inlet subcooling on two-phase heat transfer are evaluated for two surfaces: a hydrophilic surface, and a hydrophobic surface. The influence of both surface wettability and system parameters on heat transfer and CHF are evaluated.

2.1 Description of Facilities

A closed-loop facility described in Ooi et al. (2018) is modified to measure boiling heat transfer and CHF, and is shown in Figure 2.1(a). A positive-displacement pump is used to drive distilled water through the test section at a constant rate. A bypass is connected in parallel with the rest of the section to decrease pressure oscillations and to keep the flow steady through the test section. Water driven by the pump passes through a 5-kW preheater which is used to heat the water to the appropriate inlet temperature to the test section. Water is then driven into the vertical test section, a schematic of which is shown in Figure 2.1(b). The assembly is made of stainless steel except for the heater surface which is made of copper. The main section is a square channel of constant area throughout the entire assembly, measuring 12.7 mm × 12.7 mm. The unheated entry length is 490 mm followed by a one-sided heated section 107.95 mm long. The power is supplied by seven 750-W cartridge heaters connected to auto-transformers. Following the heated section, there is another 400 mm unheated section before the flow enters the condenser. The condenser cools the water to facilitate steady-state operation of the test facility. The condenser is a brazed plate heat exchanger which uses tap water on the secondary side to cool the distilled water moving through the test facility. The water then returns to the inlet of the pump, creating a closed loop.

A pressurizing tank is connected between the outlet of the condenser and the inlet of the pump. Winding vertical tubes separate the pressurizing tank from the apparatus to prevent non-condensable gases from entering the test section from the tank. The pressurizing tank is filled partially with distilled water, leaving the upper portion of the tank filled with compressible gas. A nitrogen tank and regulator are connected to the upper portion of the tank to control the system pressure. The pressurizing tank is used to control the system pressure, and it also acts to dampen pressure fluctuations.

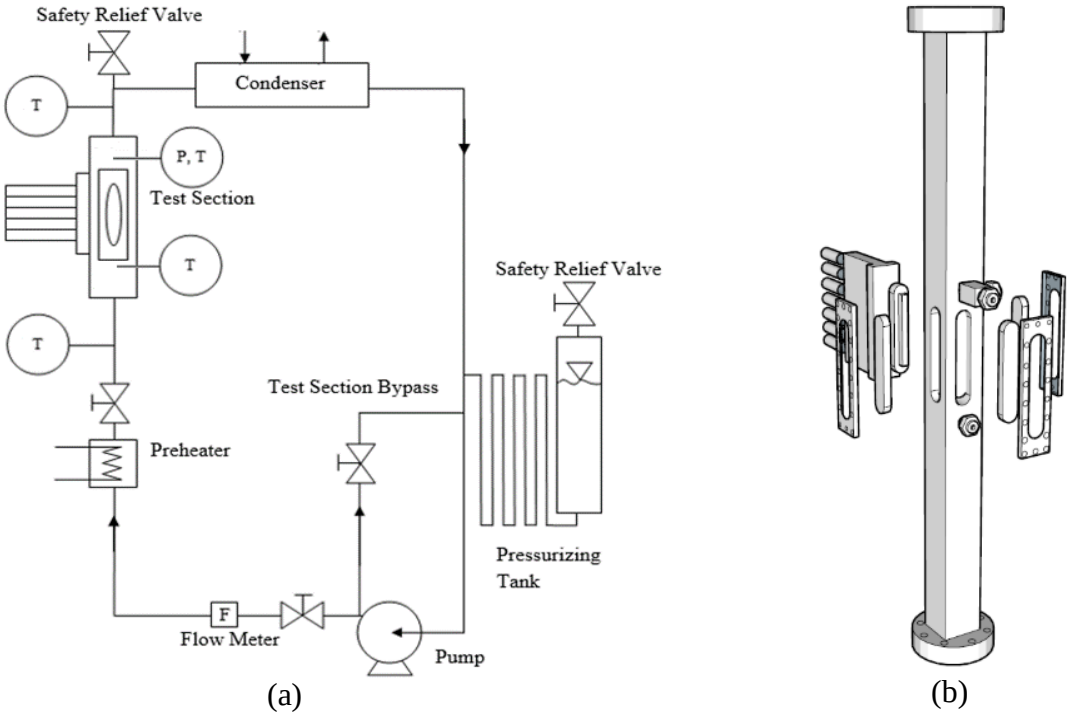

Figure 2.1 Schematic of the facility showing (a) the facility layout and (b) the test section assembly.

The flow rate is measured using a turbine flow meter downstream from the pump. The flow rate is adjusted by using the controller for the pump motor and by opening and closing the main flow control valve upstream of the main test section. The bulk fluid temperature to the test section

is controlled with a PID controller connected to the preheater based on a K-type thermocouple downstream from the preheater but upstream from the inlet to the test section assembly. Four T-type thermocouples are used within the stainless-steel test section to monitor the bulk fluid temperature at various locations. The thermocouples are placed at the beginning and end of each unheated section. The pressure transducer is connected at the end of the heated section to monitor the system pressure.

To monitor the heat flux and wall temperature of the heater surface, thermocouples were embedded into the heater surface at various depths, as shown in Figure 2.2(a). Using a linear regression, the heat flux is determined by calculating the temperature gradient, using the thermal conductivity of copper, and assuming one-dimensional heat conduction. Additionally, the wall temperature is extrapolated from the temperature profile. An example of this procedure is shown in Figure 2.2(b). The heat flux and wall temperature are then used to create the boiling curves for each condition.

Flow boiling experiments up to CHF were performed for two surfaces: a polished copper surface, and a copper surface textured to make the surface wettability hydrophobic. The copper was polished with 1500-grit SiC paper and washed with water and acetone. A Coherent Monaco femtosecond diode pumped laser system with linearly polarized light was used for the laser surface texturing of the copper heater, with a method similar to Hammouti et al. (2018). This laser operates at a central wavelength of 1040 nm (Full Width at Half Maximum), a pulse length 350 fs, and a maximum power of 40 W when repetition rate is set at 1 MHz. A dual-axis galvo system and an F-Theta lens with an effective focal length of 160 mm were used to steer and focus the beam over the surface. The maximum field size is 110 mm × 110 mm with an uncertainty of 15 μrad. A

schematic representation of the setup developed to perform 2D laser surface texturing is shown in Figure 2.3(a).

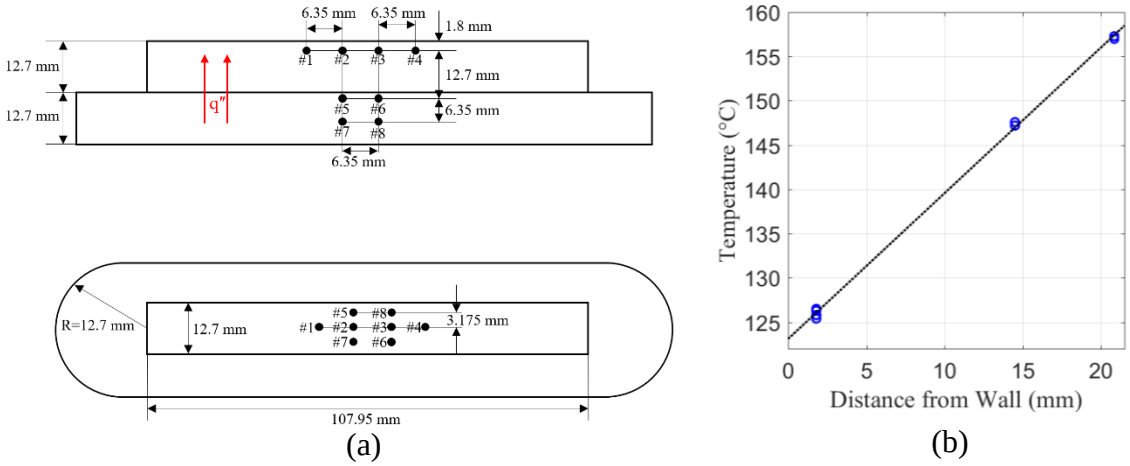

(a) (b)

Figure 2.2 (a) Heater surface with eight holes drilled for thermocouple placement and temperature measurement, and (b) sample axial temperature profile demonstrating linear temperature profile to obtain the wall temperature and heat flux

Software was developed in LabVIEW in order to control the pattern of the texturing based on an imported image. The scale of the image is directly related to the distance between impacts in both the x- and y-axes, and the number of pulses per spot corresponded to the value of each pixel which compose the image. The laser spot size was found to be approximately 40 μm. Laser power was measured and set to 10 W before the laser surface texturing by means of a high damage threshold power detector just after the F-theta lens, which leads to a fluence of 3.2 J/cm^2.

The copper surface was textured by a one-step laser process by keeping constant the lateral displacement of the laser spot at 30 μm in both the x and y directions. At each spot, 7,000 femtosecond pulses were delivered with a 1 MHz repetition rate. As shown in Figure 2.3(c), the surface which was irradiated by laser presents self-organized periodic nanostructures called ripples or LIPSS (Laser Induced Periodic Surface Structures) (Liu, 1982). The combination of these

nanostructures and the pad-like microstructures act as a multi-scale topography and is ideal for applications where hydrophobic surfaces are required.

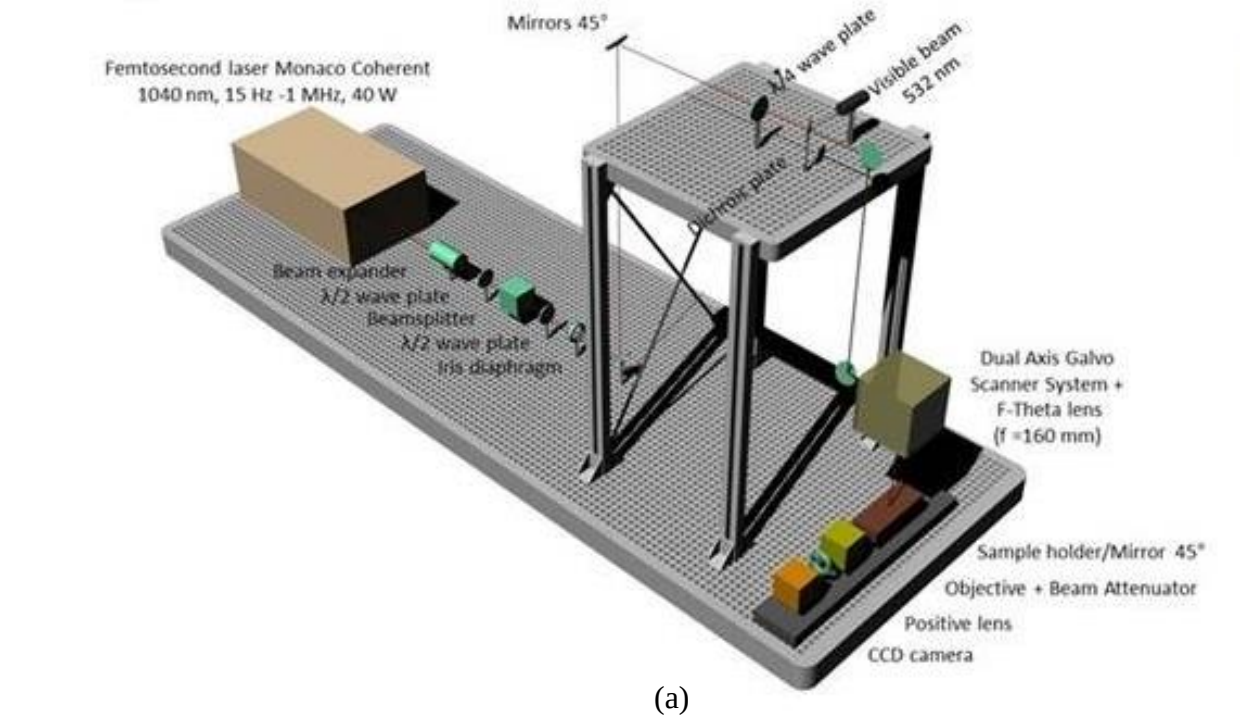

(a)

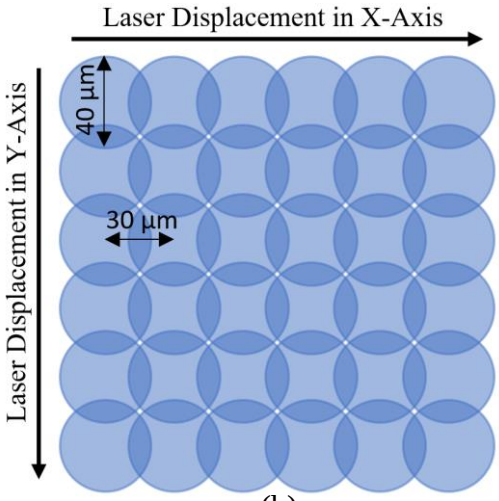

(b)

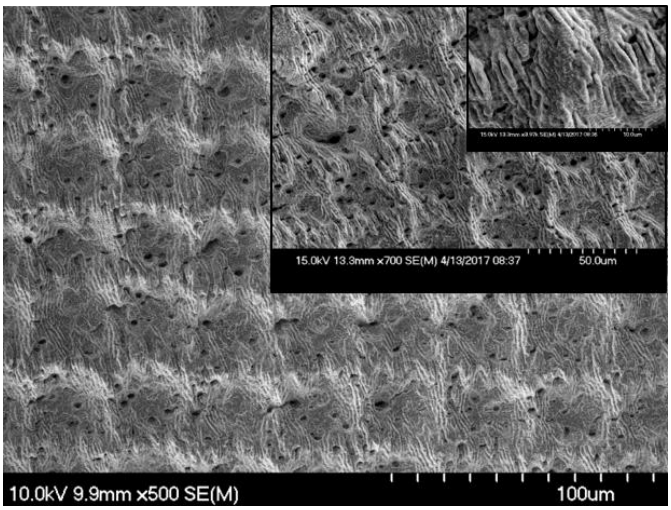

(c)

Figure 2.3 (a) Schematic representation of the setup used to perform 2D laser surface texturing. (b) The surface texturing process of the copper heater surface. (c) 20° tilted SEM image of the surface after laser treatment, inset: magnified view of the rippled topography present inside the trenches

Wettability images were taken before each surface was subjected to the twenty-one conditions. The surface wettability was characterized with Sessile drop experiments. The average was computed for each surface: for the polished copper surface, the measured contact angle was found to be 58.7±10.4°, and the measured contact angle for the textured surface was found to be 131.9±7.5°. Examples of pictures from the drop experiments are shown in Figure 2.4.

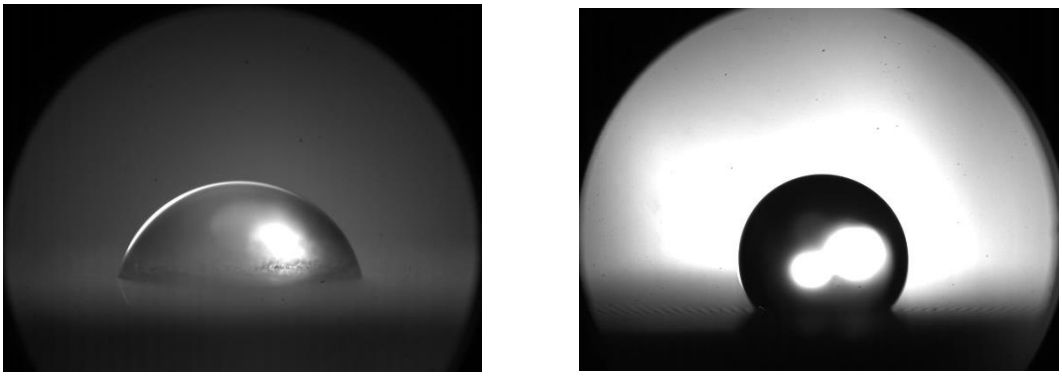

(a) (b)

Figure 2.4 Contact angle measurements on the two copper surfaces: (a) polished (hydrophilic), and (b) textured (hydrophobic)

2.2 Experimental Conditions

Conditions were set for three target pressures: 100 kPa, 225 kPa, and 350 kPa. At each of these pressures, several flow rates were set ranging between approximately 50-300 kg/m^2-s. At each flow rate, experiments were performed where the inlet was very close to saturated liquid. The two T-type thermocouples upstream from the heated section were used to ensure that the liquid entering the heated section was close to saturation but not in the two-phase region. In addition, at pressures of 100 kPa and 225 kPa, CHF excursions at several subcoolings were studied. At 100 kPa, the inlet subcooling ranged from nearly saturation to 10°C, while at 225 kPa, the inlet subcooling ranged from nearly saturation to 15°C. Table 2.1 shows the range of experimental measurements and associated uncertainty in the conditions studied. The uncertainty values for the

experimental parameters are calculated in Appendix A. The conditions were taken up in wall heater power until a rapid temperature excursion was detected at which point the heaters were turned off. A sample power profile and wall temperature profile are shown in Figure 2.5.

Table 2.1 Range of measured conditions and associated uncertainty

Experimental Parameters	Values	Experimental Uncertainty[a]
Pressure	106.0–360.1 kPa	±0.36 kPa
Inlet Subcooling	0.2–15.7 °C	±0.1 °C
Wall Superheat	0.5-23.8 °C	±0.22 °C
Mass Flux	44–285 kg/m^2-s	±6.5 kg/m^2-s
Heat Flux	25-1291 kW/m^2	±6.6 kW/m^2

[a]Based on steady-state time-averaged data

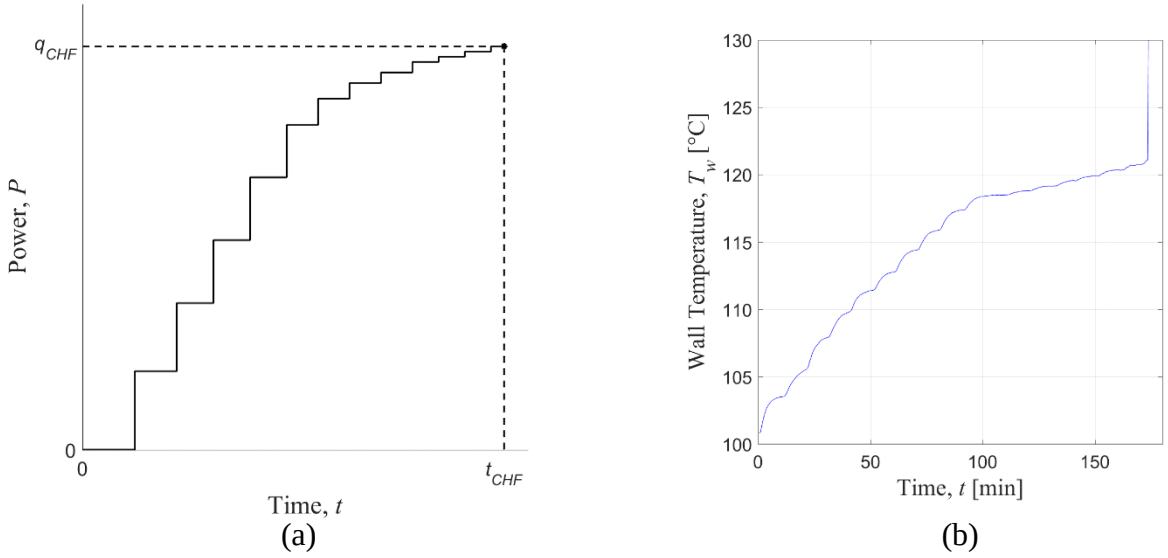

Figure 2.5 Sample input and output for a run to CHF. (a) Input of stepwise power input to cartridge heaters and (b) variation in wall temperature up to the temperature excursion point marking DNB

CHAPTER 3: RESULTS AND ANALYSIS

A total of twenty-one test conditions were performed for each copper surface with variations in the system pressure, flow rate, and inlet subcooling. The heat flux was increased in small increments until CHF was detected by a sudden increase in the wall temperature and a sudden decrease in downstream liquid temperature. The reported critical heat flux values are determined by calculating the time derivative of the wall superheat for the entire condition. A running average is then applied to the derivative to identify the point of critical heat flux from the large volume of data collected for a particular condition. The CHF is taken as the point where the derivative deviates from zero immediately before the peak in the time derivative of the wall temperature. All data after the CHF excursion is ignored due to the rapid transient nature of the phenomenon and the fact that system properties are changed in order to cool the system quickly. The data for CHF is presented along with the conditions in Table 3.1.

3.1. Flow boiling curves

The boiling curves in Figures 3.1-3.3 show three different types of data: steady-state points, running-average boiling curves between the steady-state points, and CHF excursion points. The steady-state points are depicted with markers. At these points, the heat flux and wall superheat are held constant after the system has had enough time to reach equilibrium, and the points shown are time-averaged quantities over two minutes. Next, the curves between the steady-state points are shown with solid or dotted lines. These are the boiling curves taken at 2 Hz with a running average over ten data points. Last, the CHF excursion points are shown with an arrow corresponding to the point where the temperature excursion begins.

Table 3.1 Data table with nominal reference, parameters, and critical heat flux values

Nominal Reference	P (kPa)	G (kg/m^2-s)	ΔT_{sub} (°C)	q''_{CHF} (kW/m^2)	Nominal Reference	P (kPa)	G (kg/m^2-s)	ΔT_{sub} (°C)	q''_{CHF} (kW/m^2)
Hydrophilic surface					Hydrophobic surface				
1-i	106.1	47.8	1.4	496	1-o	107.0	46.8	0.2	490
2-i	106.0	47.8	5.0	661	2-o	107.3	44.0	4.8	502
3-i	106.4	44.4	10.0	717	3-o	107.8	46.5	10.0	526
4-i	106.6	90.7	1.4	594	4-o	107.7	88.8	0.2	473
5-i	106.8	89.9	5.0	720	5-o	108.0	91.2	4.8	521
6-i	106.9	89.1	10.0	788	6-o	108.4	91.3	9.8	514
7-i	109.1	177.4	1.5	681	7-o	109.7	178.6	0.4	478
8-i	108.5	177.2	5.1	818	8-o	109.0	183.9	4.7	552
9-i	108.2	176.8	10.0	915	9-o	109.3	180.0	9.9	592
10-i	225.5	89.9	4.9	886	10-o	226.6	88.6	5.2	659
11-i	226.5	88.6	15.2	998	11-o	232.4	91.3	15.7	757
12-i	229.0	175.5	5.4	992	12-o	226.0	177.5	5.0	778
13-i	225.8	177.2	15.0	1070	13-o	228.8	177.2	15.3	918
14-i	228.8	227.7	5.3	1014	14-o	234.3	232.8	6.0	857
15-i	229.6	227.4	15.4	1290	15-o	224.8	231.7	14.9	916
16-i	227.7	278.3	5.2	1070	16-o	224.9	283.5	5.1	821
17-i	226.0	279.8	14.9	1291	17-o	223.2	285.2	14.5	907
18-i	358.0	88.6	1.1	829	18-o	357.6	91.0	1.2	903
19-i	354.1	175.7	0.4	908	19-o	360.1	176.5	1.4	971
20-i	352.7	225.9	0.7	982	20-o	356.5	228.9	1.4	1014
21-i	357.4	276.4	1.0	1145	21-o	357.1	278.6	1.3	1057

Figure 3.1 shows various boiling curves separated by mass flux for both the hydrophilic (solid line) and hydrophobic surfaces (dashed line). The boiling curves for the hydrophilic surface are consistent across different flow rates for similar pressure and subcooling conditions. The only difference among the boiling curves for the hydrophilic surface is the location of the CHF point along the boiling curve in the nucleate boiling region. At elevated flow rates, the CHF is higher; however, the slopes of the boiling curves are nearly parallel, indicating similar boiling phenomenon. The hydrophobic surface boiling curves are shifted to the right as a result of a delay in the onset of nucleate boiling relative to the hydrophilic surface. The ONB point is

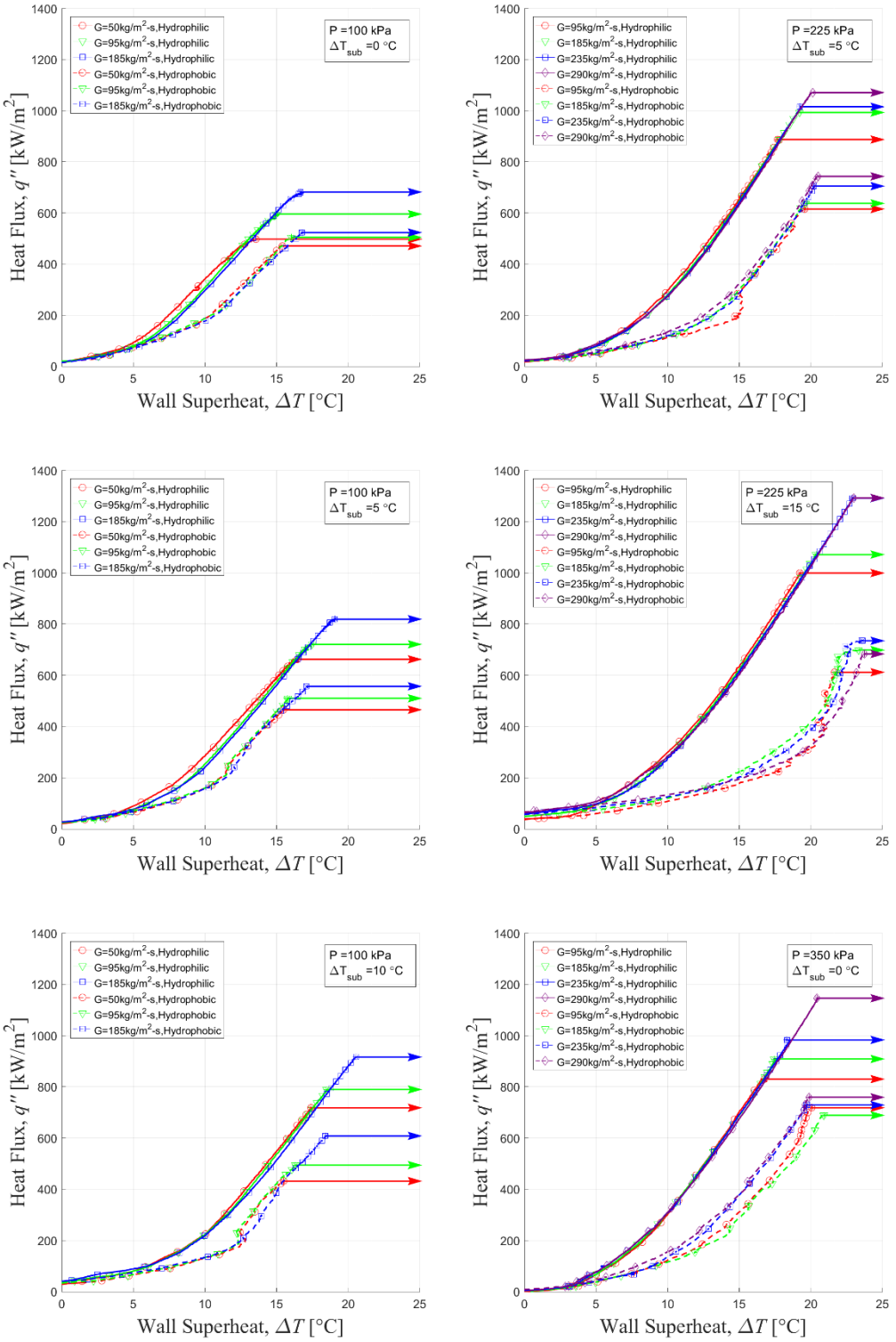

Figure 3.1 Boiling curves and CHF excursions separated by flow rate for similar pressure and subcooling conditions for two wettability surfaces

determined qualitatively from a change in the slope indicating a change from the single-phase convection region to the nucleate boiling heat transfer region. This effect of delaying the ONB point is most pronounced for the intermediate pressure condition and does not change substantially across the range of subcooling considered. Decreasing surface wettability in pool boiling has been reported to shift the ONB point to lower wall superheat (Bourdon et al., 2013; Betz et al., 2013). This difference in trend between pool and flow boiling should be investigated further. As with the hydrophilic surface, the effect of flow rate on the hydrophobic surface is shown by the delay in temperature excursion and the increase in CHF at higher flow rates for the same pressure and subcooling conditions. However, for every condition tested, the CHF for the hydrophobic surface is lower than for the hydrophilic surface.

The effect of subcooling on the boiling curves is different, however, and is shown in Figure 3.2. For the hydrophilic surface at low pressure, increasing subcooling has the effect of delaying the ONB point thus shifting boiling curves to the right. This result is most pronounced at low pressure. Elevated pressure conditions also exhibit this trend, though the effect is not as prominent. The boiling curves continue parallel to one another indicating similar boiling phenomenon for different subcoolings with similar flow rate and pressure conditions for the hydrophilic surface. For the hydrophobic surface, a similar trend is observed with the delay of the ONB point and the shift of the boiling curves to the right with increasing subcooling. At lower pressure and lower flow rate, the curves collapse on one another, and the subcooling has little effect beyond the ONB point. The CHF points are all similar for the hydrophobic surface at low mass flux, but at the higher mass flux of 200 kg/m^2-s the effect of subcooling on the CHF point is present. Likewise, for the hydrophobic surface at elevated pressures, greater subcooling delays the ONB point and shifts the

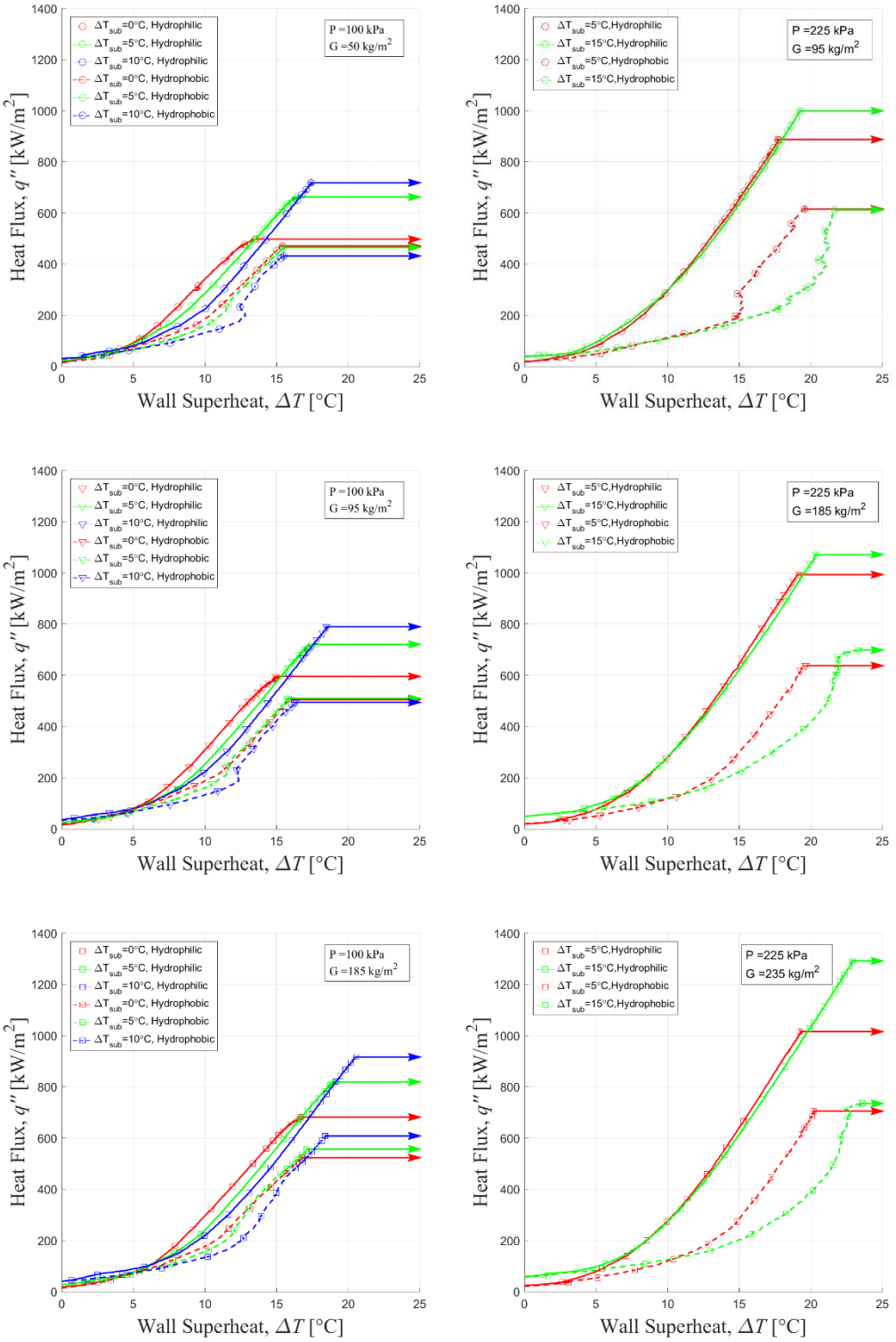

Figure 3.2 Boiling curves and CHF excursions separated by subcooling for similar pressure and flow rate conditions for two wettability surfaces

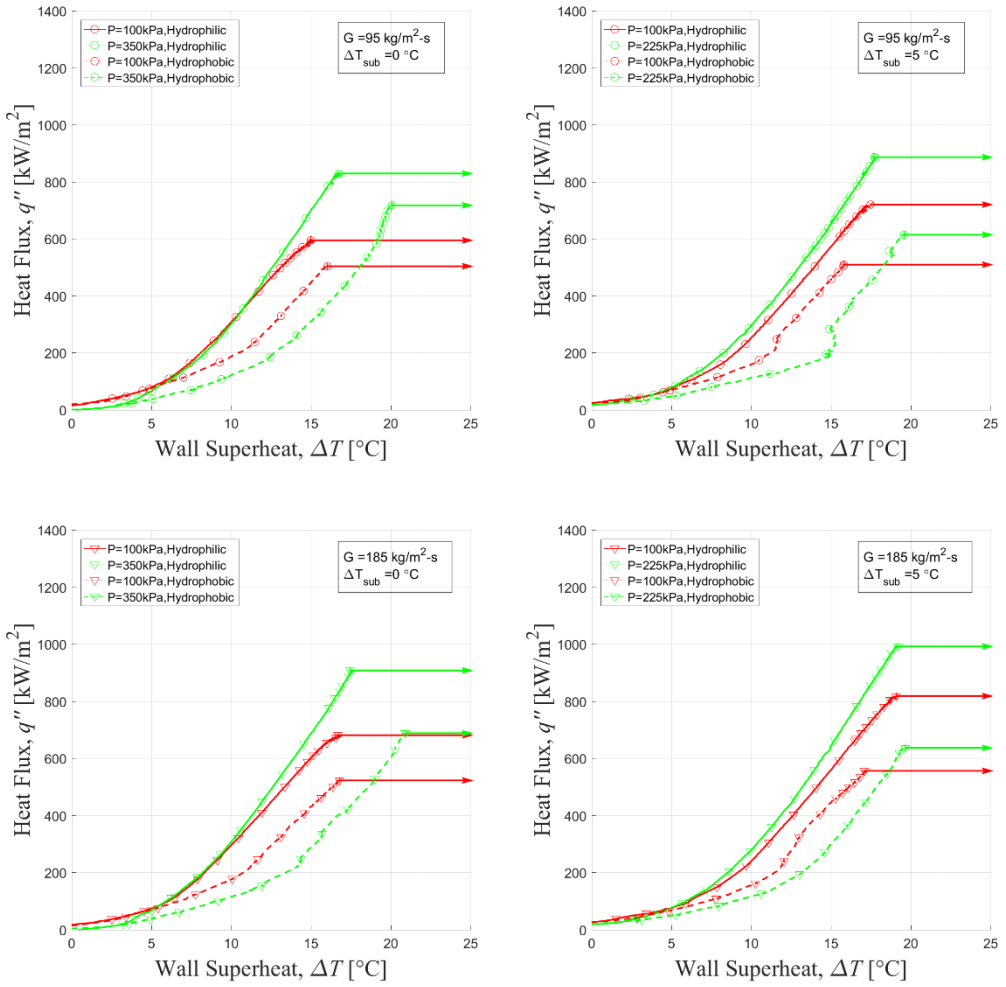

Figure 3.3 Boiling curves and CHF excursions separated by pressure for similar flow rate and subcooling conditions for two wettability surfaces

curve to the right. At elevated pressure conditions, the difference in the boiling curves between hydrophobic and hydrophilic surfaces is greater than at lower pressures. For the hydrophobic surface at elevated pressure, the effect of subcooling is not as influential on the CHF point as it is on the hydrophilic surface.

The boiling curves separated by pressure are shown in Figure 3.3. For the hydrophilic surface, increasing pressure has the effect of shifting the boiling curve to the left and increasing the CHF point. However, for the hydrophobic surface, increasing pressure has the effect of shifting

the boiling curve to the right and also increasing the CHF point. Pressure is the only of the three parameters studied to have the opposite effect on the boiling curves between the hydrophobic and hydrophilic surfaces. Flow rate and subcooling shift the CHF and the boiling curves in the same direction for the two wettabilities, but the boiling curves shift in opposite directions with increasing pressure, depending on the wettability of the heater surface. The increase in CHF is substantial for both the hydrophilic and hydrophobic cases with increasing pressure.

3.2. Critical heat flux

Figure 3.4 compiles the CHF values from the boiling curves to analyze the trend with individual system parameters. In each subfigure, different line colors and marker styles are used to separate the flow rates, pressures, and subcoolings for the cases tested. The CHF values are consistently lower for the hydrophobic surface compared to the hydrophilic surface averaging a decrease of 28% for similar system and flow conditions. It has been widely observed in pool boiling experiments that decreasing wettability decreases the CHF (Kandlikar, 2001; Hsu and Chen, 2012; Jo et al., 2011), which was also observed in flow boiling experiments by Sarwar et al. (2007). Of the system parameters, the critical heat flux is impacted the most by pressure for both surfaces but is also affected by subcooling and flow rate over the range of conditions studied. In Figure 3.4a, pressure is shown to be more influential on the CHF value for the hydrophobic surface than for the hydrophilic surface, and in some cases the CHF for the hydrophobic surface doubles from 1.0 to 3.5 atmospheres of system pressure. By comparison, the CHF for the hydrophilic surface is a strong yet more modest function of pressure. Although the CHF for the hydrophobic surface is a stronger function of pressure, the CHF for the hydrophilic surface is a strong function

of both mass flux and inlet subcooling for the range of conditions studied, as shown in Figures 3.4b and 3.4c.

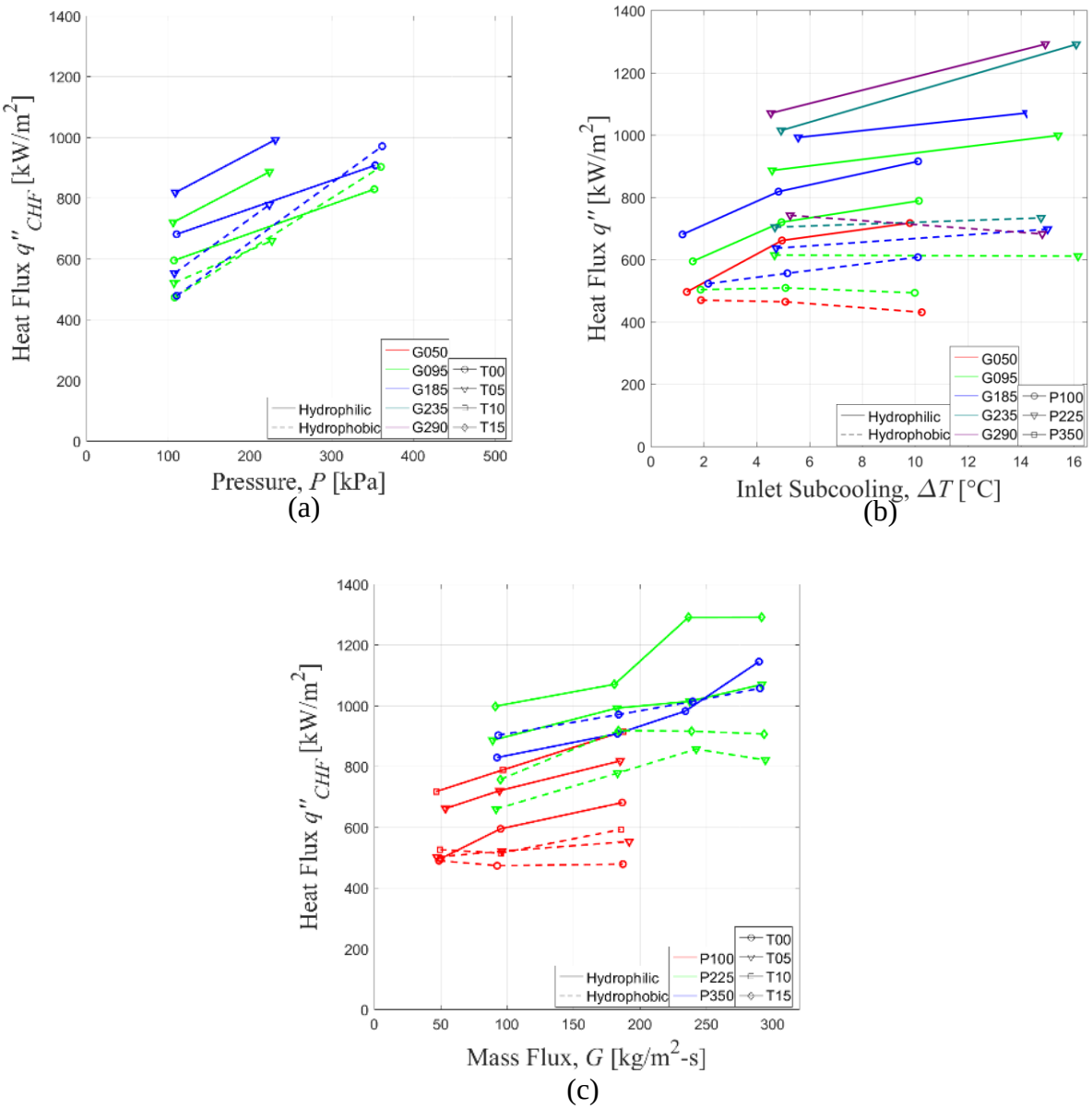

Figure 3.4 Critical heat flux values versus system parameters, (a) pressure, (b) inlet subcooling, and (c) mass flux for the two wettability surfaces

As a general trend within the range of conditions studied, CHF increasing with increasing pressure, subcooling, and mass flux has been long-accepted in flow boiling (Mishima and

Nishihara, 1987; Chun et al., 2001; Schoesse et al., 1997; El-Genk et al., 1988; Park et al., 1998; Kim et al., 2000; Lu et al., 2014; Mayer et al., 2016). In addition, under low-flow conditions, inlet subcooling was found to not be a significant influence on CHF for annular geometries (Chun et al., 2001; Schoesse et al., 1997; El-Genk et al., 1988). For the hydrophilic surface studied by Park et al. (1998), a minor influence of subcooling on CHF was observed but the dominant effect on CHF was found to be mass flux. In the present study, an independence of CHF with subcooling at low flow is only observed for the hydrophobic surface at the lowest pressure with a similar dependence on mass flux for both surfaces. This suggests the surface wettability influences the CHF transition not only in value but also in mechanism as the effect is not observed in the studied parameter range for the hydrophilic surface.

3.3. CHF model comparison

The critical heat flux data for both the hydrophilic surface and the hydrophobic surface are compared with available CHF models. The results are shown in Table 3.2 with mean errors and mean absolute errors for each data set. Many of the correlations are based on the semi-empirical models of Kutateladze (1952) and Zuber (1959) for pool boiling, so the effect of flow rate is not incorporated. Kandlikar (2001) is the only model which incorporates contact angle, a model that is based on the pool boiling correlations of Kutateladze (1952) and Zuber (1959) as well. The correlation employed by TRACE (2013) is a modified version of the Groeneveld (1996) lookup table which, at low-flow conditions, interpolates CHF based on the Zuber (1959) model. The model employed by RELAP5 (2010) is based on correlations developed by the Nuclear Research Institute Rez in the Czech Republic (1995). The RELAP5 (2010) model includes the effects of

flow rate, pressure, quality, and inlet subcooling, but there is no influence of contact angle or surface effects.

Table 3.2 Critical heat flux model comparison with experimental data

Model	ϵ_{phil}	ϵ_{phob}	$\lvert\epsilon_{phil}\rvert$	$\lvert\epsilon_{phob}\rvert$
Kandlikar (2001)	-1.0%	64.2%	19.5%	64.2%
Thorgerson (1974)	-9.4%	-50.4%	23.5%	50.5%
Lu et al. (2014)	26.8%	0.2%	26.8%	21.5%
RELAP5 (2010)	-26.9%	-72.8%	28.5%	72.8%
TRACE (2013)	-61.7%	-118.8%	62.8%	118.8%
Zuber (1959)	-55.7%	-110.0%	55.7%	110.0%
Kutateladze (1952)	-68.1%	-126.8%	68.1%	126.8%
Sudo et al. (1985)	-71.8%	-132.4%	71.8%	132.4%
Mishima et al. (1983)	-73.1%	-134.5%	73.1%	134.5%
Borishanskii (1956)	-82.0%	-146.0%	82.0%	146.0%
Chang and Snyder (1960)	-86.7%	-152.3%	86.7%	152.3%
Ivey and Morris (1962)	-86.7%	-152.3%	86.7%	152.3%
Rohsenow and Griffith (1955)	-96.0%	-165.7%	96.0%	165.7%
Zuber et al. (1962)	-111.7%	-193.8%	111.7%	193.8%
Moissis and Berenson (1963)	-114.2%	-190.4%	114.2%	190.4%
Wallis (1959)	-141.9%	-228.5%	141.9%	228.5%
Mirshak et al. (1959)	-162.4%	-258.0%	162.4%	258.0%
Katto (1981)	-169.5%	-280.9%	169.5%	280.9%
Mishima and Ishii (1984)	-185.6%	-299.0%	185.6%	299.0%
Janssen and Levy (1962)	-314.8%	-471.1%	314.8%	471.1%
Jens and Lottes (1951)	-364.5%	-568.7%	364.5%	568.7%
Biasi et al. (1967)	-417.9%	-577.7%	428.7%	596.2%
Tong (1967)	-638.5%	-917.4%	638.5%	917.4%
Bowring (1972)	-679.4%	-975.5%	955.0%	1360.8%

Nearly all of the reported correlations overpredict the observed critical heat flux for both the hydrophilic and hydrophobic surfaces. Since contact angle is not considered in the models and since the observed critical heat flux is lower for the hydrophobic surface than the hydrophilic surface, the errors are larger for the hydrophobic surface. The only exceptions to this are the correlations by Kandlikar (2001) and Lu (2014). The correlation by Kandlikar (2001) includes contact angle, but the effect is exaggerated for low-wetting surfaces, resulting in an

underestimation of CHF for the hydrophobic surface. The data the Kandlikar (2001) correlation is based off varies contact angle only from 20° to 110° for pool boiling conditions, and the effect is extrapolated for superhydrophilic surfaces and more hydrophobic surfaces. The present study has a hydrophobic surface with a contact angle of 132°, which is outside the data range considered by Kandlikar (2001). Lu (2014) is the only reported correlation to underpredict the CHF for both the hydrophobic and hydrophilic surfaces. The correlation by Lu (2014) includes the effects of geometry, pressure, and flow rate, but does not include the influence of contact angle or inlet subcooling on the CHF value. The data from which the Lu (2014) correlation is based covers a similar parameter range to the current study; however, the geometry studied was an annulus with smaller hydraulic diameter and heated length. As discovered by El-Genk (1988), heater size has an influence on the CHF, albeit to a smaller degree compared to the other system and flow parameters. Figure 3.5 shows a comparison of the experimental data and the model data for the best four reported models. The data are separated by pressure as this is the most influential factor for many of the models. Both Thorgerson (1974) and RELAP5 (2010) estimate the CHF values better than many of the other models. RELAP5 incorporates the mass flux, exit quality, and pressure and overestimates the CHF value for the hydrophilic surface and, therefore, overestimates the hydrophobic surface to a greater degree. The model by Thorgerson (1974) is an empirical model incorporating liquid velocity, pressure, and fluid temperature. Nearly every model implemented overestimates the critical heat flux, a real danger should these models be applied in low-pressure, low-flow systems. Even Kandlikar (2001), which does incorporate contact angle, struggles to capture the effect of wettability for the studied hydrophobic surface. Additional flow boiling CHF models incorporating contact angle should be developed, but in that absence, the Lu

(2014) model should be applied for conservative safety margins when operating within the range of conditions considered in this experimental study.

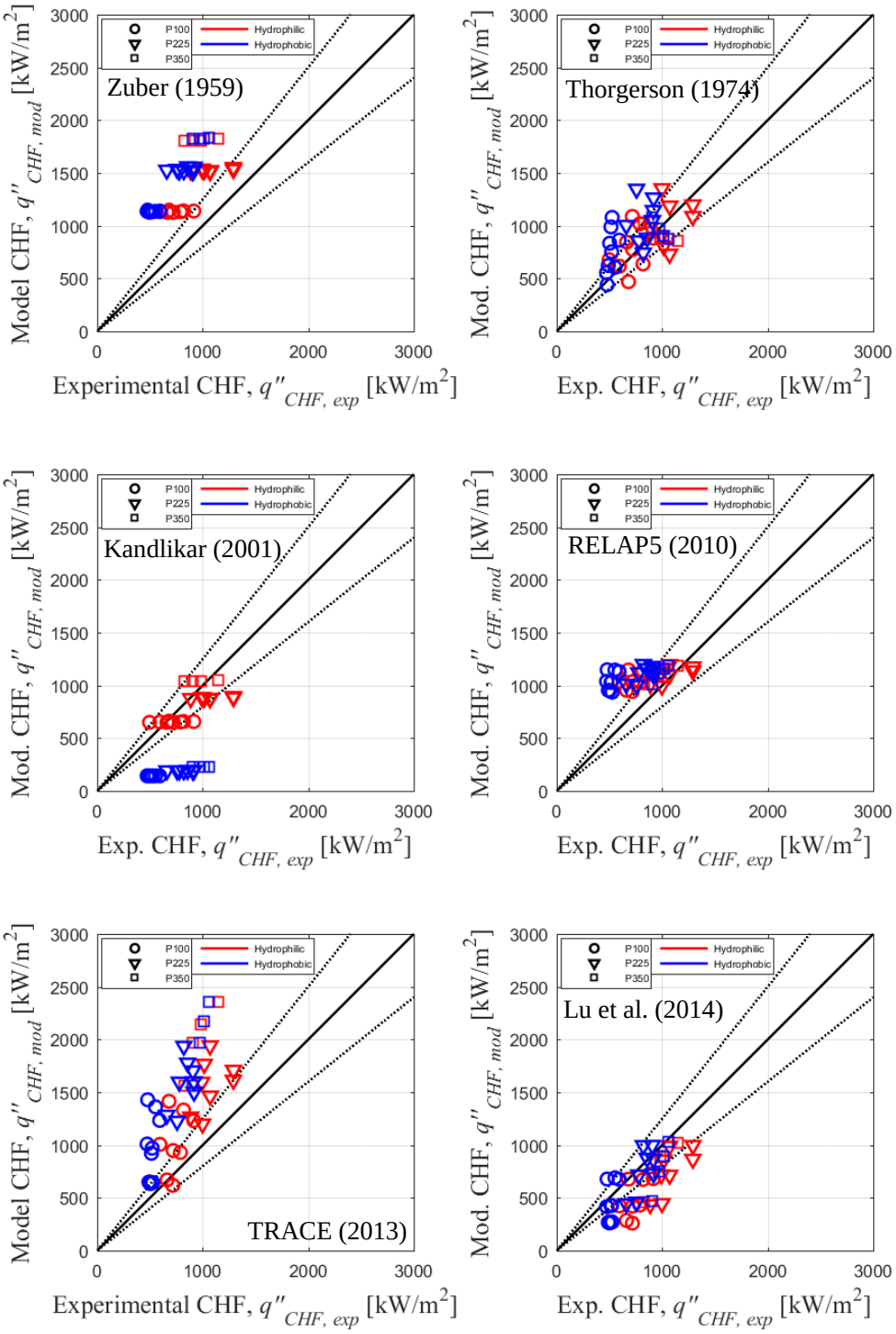

Figure 3.5 Critical heat flux data comparison with top-performing models

CHAPTER 4: CONCLUSIONS AND FUTURE WORK

It is demonstrated that wettability plays a significant role in vertical boiling flow and influences various boiling characteristics. The ONB point is delayed for every condition studied for the hydrophobic surface compared with the hydrophilic surface. In addition, the CHF is lower for every condition for the hydrophobic surface compared with the hydrophilic surface. However, similar trends are observed between conditions across the two surfaces such as similar boiling curves with changing mass flux and subcooling. Both surfaces exhibited a dependence between the CHF value and the mass flux and pressure; however, only the hydrophilic surface CHF value increased with increasing subcooling for the range of conditions considered. The small influence of inlet subcooling may be similar to the effect observed by Park et al. (1988) which was only observed in the low-flow region. As the trends are different between the two wettability surfaces, it is recommended to expand the range of conditions, particular flow rate for the hydrophobic case, in order to observe the influence of inlet subcooling on the hydrophobic CHF values.

Additional theoretical models are needed that incorporate the effect of surface wettability on boiling heat transfer. Since the wettability directly affects the multiphase boundary at the wall, models for heat transfer and CHF should incorporate these effects. The surface wetting characteristics directly affect the nucleation process, so departure frequency, departure diameter, and nucleation site density change with the surface wettability. Hydrophobic surfaces impair the ability for liquids to rewet the surface following a bubble departure which may be a significant factor in the Near-Wall Bubble Crowding Model (Hebel et al., 1981; Weisman and Pei, 1983) and the Liquid Sublayer Dryout Model (Katto, 1970; Haramura and Katto, 1983; Lee and Mudawar, 1988; Celata et al., 1994).

Models systematically overestimate the CHF point, and the only model that incorporates contact angle does not perform well. The Kandlikar (2001) CHF model modifies the Zuber (1952) model of hydrodynamic instability, but the expected CHF value becomes zero at a contact angle of 180°. Since Kandlikar (2001), the fabrication of superhydrophobic surfaces has been demonstrated, and the CHF values decrease but do not approach zero as the contact angle approaches 180°. The Kandlikar (2001) CHF model incorporating contact angle should be adjusted so that the extreme values for superhydrophobic surfaces coincide with a more reasonable limit, such as the ONB point, rather than zero heat flux. Given the catastrophic consequences that can accompany CHF, conservatism is necessary in applying these models. In summary, wettability is an important property not typically accounted for in boiling models. The surface preparation, principally the contact angle, influence the ONB point and affect the CHF value substantially, and conservatism is recommended when applying the CHF models to systems where the wettability may be changed.

REFERENCES

Bergles, A.E., Rohsenow, W.M., "The Determination of Forced-Convection Surface-Boiling Heat Transfer," *Journal of Heat Transfer*, pp. 365–372, (1964).

Betz, A.R., Jenkins, J., Kim, C.J., Attinger, D., "Boiling heat transfer on superhydrophilic, superhydrophobic, and superbiphilic surfaces," *Int. J. Heat Mass Transf.*, **57**, pp. 733–741 (2013).

Biasi, L., Clerici, G.C., Garribba, S., Sala, R., Tozzi, A., "Studies on burnout Part 3," *Energia Nucleare*, **14**(9), pp. 530–536, (1967).

Borishanskii, V. M., "An equation generalizing experimental data on the cessation of bubble boiling in a large volume of liquid, *Zh. Tekh. Fiz.*, **26**, pp. 452–456, (1956).

Bourdon, B., Marco, P.D., Rioboo, R., Marengo, M., Coninck, J.D., "Enhancing the onset of pool boiling by wettability modification on nanometrically smooth surfaces," *Int. Comm. in Heat and Mass Transf.*, **45**, pp. 11–15, (2013).

Bowring, R. W., "A simple but accurate round tube, uniform heat flux dryout correlation over the pressure range 0.7 to 17 MPa," *UKAEA*, AEEW-*R*-789, (1972).

Buividas, R., Mikutis, M., Juodkazis, S., "Surface and bulk structuring of materials by ripples with long and short laser pulses: Recent advances," *Progress in Quantum Electronics*, **38**, pp. 119–156, (2014).

Celata, G.P., Cumo, M., Mariani, A., Simoncini, M., Zummo, G., "Rationalization of existing mechanistic models for the prediction of water subcooled flow boiling critical heat flux," *Int. J. Heat Mass Transf.*, **37**(1), pp. 347–360, (1994).

Chang, Y. P., Snyder, N. W., "Heat transfer in saturated boiling," *Chem. Eng. Prog.*, **56**(30), pp. 25–28, (1960).

Chun, S.Y., Chung, H.J., Moon, S.K., Yang, S.K., Chung, M.K., Schoesse, T., Aritomi, M., "Effect of pressure on critical heat flux in uniformly heated vertical annulus under low flow conditions," *Nuclear Engineering and Design*, **203**, pp. 159–174, (2001).

El-Genk, M.S., Haynes, S.J., Kim, S.H., “Experimental studies of critical heat flux for low flow of water in vertical annuli at near atmospheric pressure,” *Int. J. Heat Mass Transf.,* **31**(11), pp. 2291–2304, (1988).

Frost, W., Kippenhan, C.J., “Bubble Growth and Heat-Transfer Mechanisms in the Forced Convection Boiling of Water containing a Surface Active Agent,” *Int. J. Heat Mass Transf.,* **10**, pp. 931–949, (1967).

Galloway, J.E., Mudawar, I., “CHF mechanism in flow boiling from a short heated wall–II. Theoretical CHF model,” *Int. J. Heat Mass Transf.,* **36**(10), pp. 2527–2540, (1993).

Groeneveld, D.C., Leung, L.K.H., Kirillov, P.L., Bobkov, V.P., Smogalev, I.P., Vinogradov, V.N., Huang, X.C., Royer, E., “The 1995 look-up table for critical heat flux in tubes,” *Nuclear Engineering Design*, **163**, pp. 1–23, (1996).

Hall, D.D., Mudawar, I., “Critical heat flux (CHF) for water flow in tubes–I. Compilation and assessment of world CHF data,” *Int. J. Heat Mass Transf.,* **43**, pp. 2573–2604, (2000).

Haramura, Y., Katto, Y., “A new hydrodynamic model of critical heat flux, applicable widely to both pool and forced convection boiling on submerged bodies in saturated liquids,” *Int. J Heat Mass Transf.,* **26**, pp. 379–399, (1983)

Hebel, W., Detavernier, A., Decreton, M., “A contribution to the hydrodynamics of boiling crisis in a forced flow of water, *Nucl. Eng. Des.*, **64**, pp. 433–445, (1981).

Hsu, C.C., Chen, P.H., “Surface wettability effects on critical heat flux of boiling heat transfer using nanoparticle coatings,” *Int. J. Heat Mass Transf.,* **55**, pp. 3713–3719, (2012).

Ivey, H. J., Morris, D. J., “On the relevance of the vapor-liquid exchange mechanism for subcooled boiling heat transfer at high pressure,” *UKAEA*, Winfrith, (1962).

Janssen, E., Levy, S., “Burnout limit curves for boiling water reactors,” *General Electric Company*, APED-3892, (1962).

Jens, W. H., Lottes, P.A., “Analysis of heat transfer, burnout, pressure drop and density data for high-pressure water,” *Argonne National Lab*, ANL-4627, (1951).

Jo, H.J., Ahn, H.S., Kang, S.H., Kim, M.H., "A study of nucleate boiling heat transfer on hydrophilic, hydrophobic and heterogeneous wetting surfaces," *Int J. Heat Mass Transf.*, **54**, pp. 5643–5652, (2011).

Kandlikar, S.G., "A Theoretical Model to Predict Pool Boiling CHF Incorporating Effects of Contact Angle and Orientation," *Journal of Heat Transfer*, **123**, pp. 1071–1079, (2001).

Katto, Y., "General Features of CHF of Forced Convection Boiling in Uniformly Heated Rectangular Channels," *Int. J. Heat Mass Transf.*, **24**(8), pp. 1413–1419, (1981).

Katto, Y., "A physical approach to critical heat flux of subcooled flow boiling in round tubes," *Int. J. Heat Mass Transf.*, **33**(4), pp. 611–620, (1990).

Kim, H.C., Baek, W.P., Chang, S.H., "Critical heat flux of water in vertical round tubes at low pressure and low flow conditions," *Nuclear Engineering and Design*, **199**, pp. 49–73, (2000).

Kim, J.M., Kang, S.H., Yu, D.I., Park, H.S., Moriyama, K., Kim, M.H., "Smart surface in flow boiling: Spontaneous change of wettability," *Int. J. Heat Mass Transf.*, **105**, pp. 147–156, (2017).

Kolev, N.I., "To the nucleate boiling theory", *Nucl Eng. Des.*, **239**, pp. 187–192, (2009).

Kumar, C.S.S., Suresh, S., Yang, L., Yang, Q., Aravind, S., "Flow boiling heat transfer enhancement using carbon nanotube coatings," *Applied Thermal Engineering*, **65**, pp. 166–175, (2014).

Kutateladze, S.S., "Heat transfer in condensation and boiling," *USAEC Report AEC-tr-3770*, (1952).

Lee, C.H., Mudawar, I., "A Mechanistic Critical Heat Flux Model for Subcooled Flow Boiling based on Local Bulk Flow Conditions," *Int. J. Multiphase Flow*, **14**(6), pp. 711–728, (1988).

Li, Y.Y., Liu, Z.H., Wang, G.S., "A predictive model of nucleate pool boiling on heated hydrophilic surfaces," *Int. J. Heat Mass Transf.*, **65**, pp. 789–797, (2013).

Lienhard, J.H., Dhir, V.K., "Hydrodynamic prediction of peak pool boiling," *J. Heat Mass Transf.*, **95**, pp. 152–158, (1973).

Lin, M., Chen, P., "Photographic study of bubble behavior in subcooled flow boiling using R-134a at low pressure range," *Annals of Nuclear Energy*, **49**, pp. 23–32, (2012).

Liu, J.M., “Simple technique for measurements of pulsed Gaussian-beam spot sizes,” *Optics Letters*, **7**(5), pp. 196–198, (1982).

Lu, D., Wen, Q., Liu, T., Su, Q., “A critical heat flux experiment with water flow at low pressures in thin rectangular channels,” *Nuclear Engineering and Design*, **278**, pp. 669–678, (2014).

Marcel, C., Clausse, A., Frankiewicz, C., Betz, A., Attinger, D., “Numerical investivation into the effect of surface wettability in pool boiling heat transfer with a stochastic-automata model,” *Int J. Heat Mass Transf.*, **111**, pp. 657–665, (2017).

Mayer, G., Nagy, R., Nagy, I., “An experimental study on critical heat flux in vertical annulus under low flow and low pressure conditions,” *Nuclear Engineering and Design*, **310**, pp. 461–469, (2016).

Mirshak, S., Durant, W.S., Towell, R.H., “Heat Flux at Burnout,” *Savannah River Laboratory*, (1959).

Mishima, K., Ishii, M., “Flow regime transition criteria for upward two-phase flow in vertical tubes,” *Int. J. Heat Mass Transf.*, **27**(5), pp. 723–737, (1984).

Mishima, K., Nishihara, H., Shibata, T., “CHF correlations related to the core cooling of a research reactor,” *Proc. Int. Mtg. on reduced enrichment for research and test reactors*, Tokai, Japan, (1983).

Mishima, K., Nishihara, H., “Effect of channel geometry on critical heat flux for low pressure water,” *Int. J. Heat Mass Transf.*, **30**(6), pp. 1169–1182, (1987).

Moissis, R., Berenson, P. J., “On the Hydrodynamic Transitions in Nucleate Boiling,” *Journal of Heat Transfer*, **85**(3), pp. 221–229, (1963).

Mudawar, I., Howard, A.H., Gersey, C.O., “An analytical model for near-saturated pool boiling critical heat flux on vertical surfaces,” *Int. J. Heat Mass Transf.*, **40**(10), pp. 2327–2339, (1997).

Park, C., Chang, S.H., Baek, W.P., “Critical heat flux for finned and unfinned geometries under low flow and low pressure conditions,” *Nuclear Engineering and Design*, **183**, pp. 235–247, (1998).

Pernica, R., Cizek, J., “General Correlation for Prediction of Critical Heat Flux Ratio,” *Proceedings of the 7th International Meeting on Nuclear Reactor Thermal-Hydraulics, NURETH-7*, NUREG/CP-0142, **4**, Saratoga Springs, NY, (1995).

Quan, X., Dong, L, Cheng, P., "A CHF model for saturated pool boiling on a heated surface with micro/nano-scale structures," *Int. J. Heat Mass Transf.*, **76**, pp. 452–458, (2014).

"RELAP3.3 MOD3.3 Code Manual Volume IV: Models and Correlations," *Information Systems Laboratories, Inc.*, Rockville, Maryland, Idaho Falls, Idaho, (2010).

Rohsenow, W.M., Griffith, P., "Correlation of Maximum Heat Flux Data for Boiling of Saturated Liquids," *Massachusetts Institute of Technology, Division of Industrial Cooperation*, (1955).

Sakashita, H., Ono, A., "Boiling behaviours and critical heat flux on a horizontal plate in saturated pool boiling of water at high pressures," *Int. J. Heat Mass Transf.*, **52**, pp. 744–750, (2009).

Sarwar, M.S., Jeong, Y.H., Chang, S.H., "Subcooled flow boiling CHF enhancement with porous surface coatings," *Int. J. Heat Mass Transf.*, **50**, pp. 3649–3657, (2007).

Schoesse, T., Aritomi, M., Kataoka, Y., Lee, S.R., Yoshioka, Y., Chung, M.K., "Critical Heat Flux in a Vertical Annulus under Low Upward Flow and near Atmospheric Pressure," *Journal of Nuclear Science and Technology*, **34**(6), pp. 559–570, (1997).

Sommers, A.D., Yerkes, K.L., "Using micro-structural surface features to enhance the convective flow boiling heat transfer of R-134a on aluminum," *Int. J. Heat Mass Transf.*, **64**, pp. 1053–1063, (2013).

Sudo, Y., Miyata, K., Ikawa, H., Kaminaga, M., Ohkawara, M., "Experimental Study of Differences in DNB Heat Flux between Upflow and Downflow in Vertical Rectangular Channel. *Journal of Nuclear Science and Technology*, **22**(8), pp. 604–618, (1985).

Thorgerson, E.J., Knoebel, D.H., Gibbons, J.H., "A Model to Predict Convective Subcooled Critical Heat Flux," *Journal of Heat Transfer*, **96**, pp. 79–82, (1974).

Tong, L.S., "Prediction of departure from nucleate boiling for an axially non-uniform heat flux distribution," *Journal of Nuclear Energy*, **21**(3), pp. 241–248, (1967).

"TRACE V5.840 Theory Manual: Field Equations, Solution Methods, and Physical Models," Division of Safety Analysis, Office of Nuclear Regulatory Research, *U.S. Nuclear Regulatory Commission*, Washington, DC, (2013).

Wallis, G.B., "Flooding velocities for air and water in vertical tubes," *AEEW-R123*, (1961).

Wang, C.H., Dhir, V.K., “Effect of surface wettability on active nucleation site density during pool boiling of saturated water,” *J. Heat Transf.*, **115**, pp. 659–669, (1993).

Weatherhead, R.J., “Nucleate Boiling Characteristics and the Critical Heat Flux Occurrence in Subcooled Axial-Flow Water Systems”, *ANL-6675*, Argonne National Laboratory, Argonne, IL, (1963).

Weisman, J., Pei, B.S., “Prediction of Critical Heat Flux in Flow Boiling at Low Qualities,” *Int. J. Heat Mass Transf.*, **26**(10), pp. 1463–1477, (1983).

Zuber, N., “Hydrodynamic Aspects of Boiling Heat Transfer,” Ph.D. thesis, Research Laboratory, *Los Angeles and Ramo-Wooldridge Corporation*, University of California, Los Angeles, CA, (1959).

Zuber, N., Tribus, M., Westwater, J.W., “The hydrodynamic crisis in pool boiling of saturated and subcooled liquids,” *Proc. International Conference on Developments in Heat Transfer*, ASME, New York, (1962).

APPENDIX A: UNCERTAINTY EVALUATION

Pressure

The uncertainty in the pressure measurements is based on the devices used to measure the pressure and to record the data. The pressure transducer is a RoseMount Model 3051S1C with a measurement uncertainty of 0.025% of the range. The recording device is an NI 9203 operating at a frequency of 100 Hz with a measurement uncertainty of 0.02% of the range and 0.04% of the reading. The signal passed is a current signal ranging from 4 mA to 20 mA corresponding to the lower- and upper-range values of the device. For all experiments performed with the pressure transducer, the lower and upper limits were set to 0. kPa and 600. kPa, respectively. The measurement uncertainty, taken at the maximum of the pressure range, is given,

$$\sigma_p = \sqrt{\sigma_{PT}^2 + \sigma_{NI_1}^2 + \sigma_{NI_2}^2}$$

$$\sigma_p = \sqrt{\left(16 \times 2.5 \times 10^{-4}\right)^2 + \left(16 \times 2.0 \times 10^{-4}\right)^2 + \left(20 \times 4.0 \times 10^{-4}\right)^2}\ \text{mA} \times \frac{600\ \text{kPa}}{16\ \text{mA}}$$

$$\sigma_p = 0.36\ \text{kPa}$$

Flow Rate & Mass Flux

The volumetric flow rate is measured using a Sabre Mode TRG-11.375 turbine flow meter with an accuracy of 1.0%. The signal is passed through a process monitor, an MX 9000 by AW Lake Company, with an accuracy of 0.57%. The signal is processed by an NI 9203 operating at a frequency of 100 Hz with a measurement uncertainty of 0.02% of the range and 0.04% of the reading. The signal passed is a current signal ranging from 4 mA to 20 mA corresponding to 0.0 GPM and 1.5 GPM, respectively.

$$\sigma_Q = \sqrt{\sigma_{TF}^2 + \sigma_{MX}^2 + \sigma_{NI_1}^2 + \sigma_{NI_2}^2}$$

$$\sigma_Q = \sqrt{\left(16\times1.0\times10^{-2}\right)^2 + \left(16\times5.7\times10^{-3}\right)^2 + \left(16\times2.0\times10^{-4}\right)^2 + \left(20\times4.0\times10^{-4}\right)^2}\ \text{mA} \times \frac{1.5\ \text{GPM}}{16\ \text{mA}}$$

$$\sigma_Q = 0.0173\ \text{GPM}$$

The flow rate is converted to SI and converted to a mass flux.

$$\sigma_Q = 0.0173\ \text{GPM} \times \frac{63.09\ \text{cm}^3/\text{s}}{1\quad \text{GPM}}$$

$$\sigma_Q = 1.09\ \text{cm}^3/\text{s}$$

The mass flux is given by,

$$G = \frac{\dot{m}}{A} = \frac{\rho Q}{A}$$

The maximum density used in any of the experiments is used here, which corresponds to 10°C subcooled water at atmospheric pressure,

$$\sigma_G = \frac{\rho}{A}\sigma_Q$$

$$\sigma_G = \frac{960\ \text{kg/m}^3}{1.27^2\ \text{cm}^2} \times 1.09\ \text{cm}^3/\text{s} \times \frac{1\quad \text{m}}{100\ \text{cm}}$$

$$\sigma_G = 6.5\ \text{kg}/\text{m}^2\text{-s}$$

Inlet Subcooling

The inlet fluid temperature is measured using a T-type thermocouple with an accuracy of 1.0°C. The signal is recorded with a TI 9214 at a measurement frequency of 2 Hz and a measurement accuracy of 0.37°C. The uncertainty of the inlet subcooling is, therefore,

$$\sigma_T = \sqrt{\sigma_{TC}^2 + \sigma_{NI}^2}$$

$$\sigma_T = \sqrt{1.0^2 + 0.37^2}\ \text{°C}$$

$$\sigma_T = 1.07\ ^\circ\text{C}$$

For a time-averaged point, the uncertainty is averaged over one hundred twenty points, so the uncertainty of the time-averaged points is given by,

$$\sigma_{T_{sub}} = \frac{\sigma_T}{\sqrt{N}}$$

$$\sigma_{T_{sub}} = \frac{1.07}{\sqrt{120}}\ ^\circ\text{C}$$

$$\sigma_{T_{sub}} = 0.10\ ^\circ\text{C}$$

Heat Flux & Wall Temperature

The wall temperature and temperature gradient are calculated based on the linear interpolation equations:

$$m = \frac{\sum_{i=1}^{N} x_i y_i - n\overline{xy}}{\sum_{i=1}^{N} x_i^2 - n\overline{x}^2}$$

$$b = \frac{y\sum_{i=1}^{N} x_i^2 - x\sum_{i=1}^{N} x_i y_i}{\sum_{i=1}^{N} x_i^2 - n\overline{x}^2}$$

Dividing by the number of thermocouples, n, in both the numerator and denominator,

$$m = \frac{\langle xy\rangle - \langle x\rangle\langle y\rangle}{\langle x^2\rangle - \langle x\rangle^2}$$

$$b = \frac{\langle x^2\rangle\langle y\rangle - \langle x\rangle\langle xy\rangle}{\langle x^2\rangle - \langle x\rangle^2}$$

Assuming high confidence in the x-locations relative to the y-values, the uncertainty only needs to be applied to two terms: $\langle y\rangle$ and $\langle xy\rangle$.

$$\langle y \rangle = \frac{1}{N} \sum_{i=1}^{N} y_i$$

$$\sigma_{\langle y \rangle} = \frac{1}{N} \sqrt{\sum_{i=1}^{N} \sigma_{y_i}^2}$$

$$\sigma_{\langle y \rangle} = \frac{1}{N} \sqrt{N \sigma_y^2}$$

$$\sigma_{\langle y \rangle} = \frac{\sigma_y}{\sqrt{N}}$$

Next,

$$\langle xy \rangle = \frac{1}{N} \sum_{i=1}^{N} x_i y_i$$

$$\sigma_{\langle xy \rangle} = \frac{1}{N} \sqrt{\sum_{i=1}^{N} x_i^2 \sigma_{y_i}^2}$$

$$\sigma_{\langle xy \rangle} = \frac{\sigma_y}{N} \sqrt{\sum_{i=1}^{N} x_i^2}$$

$$\sigma_{\langle xy \rangle} = \frac{\sigma_y}{N} \sqrt{N \langle x^2 \rangle}$$

$$\sigma_{\langle xy \rangle} = \sigma_y \sqrt{\frac{\langle x^2 \rangle}{N}}$$

These uncertainties are applied to the equations for slope and intercept to yield the uncertainties associated with each.

$$\sigma_m = \frac{1}{\langle x^2 \rangle - \langle x \rangle^2} \sqrt{\sigma_{\langle xy \rangle} + \sigma_{\langle y \rangle}^2 \langle x \rangle^2}$$

$$\sigma_m = \frac{1}{\langle x^2 \rangle - \langle x \rangle^2} \sqrt{\sigma_y^2 \frac{\langle x^2 \rangle}{N} + \sigma_y^2 \frac{\langle x \rangle^2}{N}}$$

$$\sigma_m = \frac{\sigma_y \sqrt{\left\langle x^2 \right\rangle + \left\langle x \right\rangle^2}}{\sqrt{N}\left(\left\langle x^2 \right\rangle - \left\langle x \right\rangle^2\right)}$$

Next, the wall temperature,

$$\sigma_b = \frac{1}{\left\langle x^2 \right\rangle - \left\langle x \right\rangle^2} \sqrt{\sigma_{\langle y \rangle}^2 \left\langle x^2 \right\rangle^2 + \sigma_{\langle xy \rangle}^2 \left\langle x \right\rangle^2}$$

$$\sigma_b = \frac{1}{\left\langle x^2 \right\rangle - \left\langle x \right\rangle^2} \sqrt{\sigma_y^2 \frac{\left\langle x^2 \right\rangle^2}{N} + \sigma_y^2 \frac{\left\langle x^2 \right\rangle \left\langle x \right\rangle^2}{N}}$$

$$\sigma_b = \frac{\sigma_y \sqrt{\left\langle x^2 \right\rangle} \sqrt{\left\langle x^2 \right\rangle + \left\langle x \right\rangle^2}}{\sqrt{N}\left(\left\langle x^2 \right\rangle - \left\langle x \right\rangle^2\right)}$$

The temperatures are measured using 8 K-type thermocouples with accuracies of 2.2°C. The temperatures are recorded using a TI 9214 at 2 Hz with an uncertainty of 0.42°C. The individual thermocouple uncertainties are therefore,

$$\sigma_T = \sqrt{\sigma_{TC}^2 + \sigma_{NI}^2}$$

$$\sigma_T = \sqrt{2.2^2 + 0.42^2}\ ^\circ\mathrm{C}$$

$$\sigma_T = 2.24\ ^\circ\mathrm{C}$$

The eight thermocouples are located at positions of 4×1.8 mm, 2×14.5 mm, and 2×20.85 mm. The average position is $\left\langle x \right\rangle = 9.74$ mm, and the average squared-position is $\left\langle x^2 \right\rangle = 162.9$ mm^2. The thermal conductivity at the operating temperature of 150°C is 385 W/m-°C. The heat flux is time-averaged over two minutes yielding one hundred twenty points, so the uncertainty in the time-averaged heat flux is,

$$\sigma_{q''} = k \times \sigma_m / \sqrt{N_t}$$

$$\sigma_{q''} = \frac{k\sigma_y \sqrt{\langle x^2 \rangle + \langle x \rangle^2}}{\sqrt{N}\sqrt{N_t}\left(\langle x^2 \rangle - \langle x \rangle^2\right)}$$

$$\sigma_{q''} = \frac{385 \times 2.24 \times \sqrt{162.9 + 9.74^2}}{\sqrt{8}\sqrt{120}\left(162.9 - 9.74^2\right)} \text{ W / m-mm-°C}$$

$$\sigma_{q''} = 6.6 \text{ kW/m}^2$$

Applying the same values to the wall temperature and neglecting the uncertainty in the saturation temperature,

$$\sigma_{\Delta T} = \frac{\sigma_y \sqrt{\langle x^2 \rangle}\sqrt{\langle x^2 \rangle + \langle x \rangle^2}}{\sqrt{N}\sqrt{N_t}\left(\langle x^2 \rangle - \langle x \rangle^2\right)}$$

$$\sigma_{\Delta T} = \frac{2.24 \times \sqrt{162.9}\sqrt{162.9 + 9.74^2}}{\sqrt{8}\sqrt{120}\left(162.9 - 9.74^2\right)} \text{ °C}$$

$$\sigma_{\Delta T} = 0.22 \text{ °C}$$